The realizable Markovian closure and realizable test-field model. II. Application to anisotropic drift-wave dynamics

John C. Bowman*
Max-Planck-Institut für Plasmaphysik, EURATOM Association, D 85748 Garching, Germany

John A. Krommes
Plasma Physics Laboratory, Princeton University, P.O. Box 451, Princeton, NJ 08543
(Received 6 February 1997; accepted 7 August 1997)

The test-field model is shown to be potentially *nonrealizable* in the presence of linear waves such as those frequently encountered in models of plasma and geophysical turbulence. A new statistical closure, the realizable test-field model (RTFM), is proposed as a remedy. Both the damping rate and frequency are renormalized to account for nonlinear damping and frequency shifts. Like the realizable Markovian closure (RMC), the RTFM is based on a modified fluctuation–dissipation ansatz. Numerical solutions of the RTFM, RMC, and direct-interaction approximation for the Hasegawa–Mima equation are presented; rough agreement with direct numerical solution is found. The number of retained Fourier modes is dramatically reduced with an anisotropic generalization of a recently developed wave-number partitioning scheme.

47.27.Eq, 52.35.Ra, 92.10.Lq

*Present address: Department of Mathematical Sciences, University of Alberta, Edmonton, Alberta, Canada T6G 2G1

I. INTRODUCTION

Over the past few decades, statistical closures have been widely used to obtain approximate but quantitative descriptions of turbulence. These analytical theories strive to close the infinite moment hierarchy that results upon averaging a stochastic nonlinear equation over an ensemble of initial conditions. Probably the most familiar example of a statistical closure is Kraichnan's direct-interaction approximation (DIA).[1–5]

In Part I of this work,[6] a serious deficiency of a popular analytical theory of turbulence, the DIA-based eddy-damped Markovian quasinormal (EDQNM) closure, was pointed out: in the presence of linear waves, that approximation can lead to (unphysical) negative energies. An alternative approximation, the realizable Markovian closure (RMC), was proposed as a remedy. Although the steady-state EDQNM and RMC equations are equivalent, the RMC provides a realizable[7,8] evolution to a saturated state. This property is crucial to any numerical implementation; without it, the closure equations can lead to violent instabilities.

There is yet another difficulty with the DIA-based EDQNM equations that is not resolved in the RMC. Like the underlying DIA equations, the EDQNM and RMC both predict a spurious interaction between the large- and small-scale eddies. The associated erroneous transfer of energy associated with this process leads to an energy spectrum that is shallower than the Kolmogorov prediction. This discrepancy is the result of a failure of the DIA equations to obey the statistical property of the primitive dynamics known as random Galilean invariance. Although this violation probably does not significantly affect the predictions of DIA-based closures at the longest wavelengths, it is a general goal of turbulence theory to recover the correct spectral behavior in each of the energy-injection, inertial, and dissipation ranges. One possible candidate that could accomplish this is a closure closely related to the DIA-based EDQNM known as the test-field model (TFM).[9,10] The TFM is invariant to random Galilean transformations of the fundamental fields; consequently it predicts the expected Kolmogorov scalings. Unfortunately, this success comes with an additional penalty: unlike DIA-based closures, the TFM contains an adjustable parameter. Substantial effort has been devoted in the literature to the search for other random-Galilean-invariant closures (see, e.g., Refs. 11–14); however, these approximations have not been extensively used (nevertheless, see Refs. 15 and 16), partly because of the inherent arbitrariness in their formulations.[17] Although these are topics that deserve further investigation, we do not pursue them here. Our primary goal is to develop a realizable version of the TFM for the Charney–Hasegawa–Mima (or simply, Hasegawa–Mima) equation, a widely-used description of drift-wave[18,19] and two-dimensional barotropic[20] turbulence.

We begin with a brief review of the RMC in Sec. II and the TFM in Sec. III. Next, we develop in Sec. IV a new closure, the realizable test-field model (RTFM). Unlike the TFM, the RTFM is guaranteed to be realizable even in the presence of the linear waves encountered in plasma and geophysical turbulence. In the wave-free case it also exhibits improved transient behavior (although in a steady state the RTFM equations typically reduce to the equations for the TFM). Unfortunately, in common with the TFM, the RTFM contains an adjustable parameter. Although it is possible to fix this constant by comparing the TFM and DIA in a situation where the DIA is considered to be reliable,[9] the need for such fitting is admittedly an undesirable weakness. For this reason, we do not completely abandon the RMC in favor of the RTFM. In the end, we have at our disposal two complementary tools for studying drift-wave turbulence: (i) a Markovian statistical closure derived systematically from the DIA, containing no adjustable constants, that predicts incorrect inertial-range dynamics; and (ii) a more heuristic approximation, involving adjustable parameters, that nevertheless yields the expected spectral behavior in an inertial range. Using these tools, one can learn much about the statistical properties of the turbulent field.

To facilitate the numerical solution of these approximations, in Sec. V we generalize a recent advance in the implementation of statistical closures to handle two-dimensional *anisotropic* turbulence. Statistical approximations are well suited to a technique of wave-number reduction that can greatly extend the inertial range over which closure solutions can be obtained. The method is based on a partitioning of wave-number space into bins over which the statistical variables are presumed to vary smoothly. Only a single representative mode is evolved from each bin. One accounts for the number of interacting modes in each triad of wave-number bins *via* certain time-independent geometrical weight factors. Since these weight factors do not involve the dynamical variables, they need to be computed only once for each new wave-number partition. The pioneering work on this technique was done by Leith and Kraichnan;[21] however, the energy spectrum predicted by their scheme converges extremely slowly as the wave-number partition is refined. The more exact treatment of the wave-number partitioning developed in Ref. 22 exhibits dramatically improved convergence and corrects the mistreatment pointed out by Pouquet[23] of nonlocal interactions in the original scheme of Leith and Kraichnan. We describe in this work an anisotropic version of the isotropic scheme presented in Ref. 22.

Next, in Secs. VI and VII we discuss the application of this work to the Hasegawa–Mima equation. Related techniques have previously been applied both to isotropic turbulence[24] and to anisotropic Terry–Horton[25] and Hasegawa–Wakatani turbulence.[26,27] However, the present work represents the first application of the RTFM (and also of the more accurate wave-number partitioning scheme developed in Ref. 22) to anisotropic turbu-

lence. Overall, the results indicate that, for systems with many interacting modes, the closures work reasonably well in comparison with direct simulations of the primitive dynamical equations. The algorithm used to compute the geometrical weight factors needed to implement the wave-number partitioning scheme is discussed in Appendix A. Finally, in Appendix B we describe the code `DIA`[28,29] that was used to obtain the closure solutions reported in this work.

II. THE REALIZABLE MARKOVIAN CLOSURE

We consider an equation for a scalar field ψ, with zero mean, that includes an advective nonlinearity of the form $\boldsymbol{v}\cdot\boldsymbol{\nabla}A\psi$, where A is a linear operator. (For example, the Hasegawa–Mima equation has this form with $\boldsymbol{v}$ being the $\boldsymbol{E}\times\boldsymbol{B}$ velocity $\hat{\boldsymbol{z}}\times\boldsymbol{\nabla}\hat{\psi}$ and $A=-\nabla_\perp^2$.) The velocity field is assumed to be determined from an auxiliary field $\hat{\psi}$ such that for passive advection ($\hat{\psi}$ specified externally) the Fourier-analyzed equation takes the form

$$\left(\frac{\partial}{\partial t}+\nu_{\boldsymbol{k}}\right)\psi_{\boldsymbol{k}}(t)=\sum_{\boldsymbol{k}+\boldsymbol{p}+\boldsymbol{q}=\boldsymbol{0}}M^U_{\boldsymbol{kpq}}\psi^*_{\boldsymbol{p}}(t)\hat{\psi}^*_{\boldsymbol{q}}(t). \tag{1}$$

Here the unsymmetrized mode-coupling coefficient $M^U_{\boldsymbol{kpq}}$, which describes advection of mode $\boldsymbol{p}$ by mode $\boldsymbol{q}$, and the complex coefficient of linear "damping" $\nu_{\boldsymbol{k}}$ are both independent of time. Knowledge of $M^U_{\boldsymbol{kpq}}$ is required for the later discussion of test-field models; however, we are actually concerned with the self-consistent problem obtained by setting $\hat{\psi}=\psi$:

$$\left(\frac{\partial}{\partial t}+\nu_{\boldsymbol{k}}\right)\psi_{\boldsymbol{k}}(t)=\tfrac{1}{2}\sum_{\boldsymbol{k}+\boldsymbol{p}+\boldsymbol{q}=\boldsymbol{0}}M_{\boldsymbol{kpq}}\psi^*_{\boldsymbol{p}}(t)\psi^*_{\boldsymbol{q}}(t), \tag{2}$$

where $M_{\boldsymbol{kpq}}\doteq M^U_{\boldsymbol{kpq}}+M^U_{\boldsymbol{kqp}}$ are symmetrized mode-coupling coefficients (we emphasize definitions with the notation $\doteq$).

For some time-independent nonrandom real quantity $\sigma_{\boldsymbol{k}}$, the $M_{\boldsymbol{kpq}}$ typically satisfy a further symmetry of the form

$$\sigma_{\boldsymbol{k}}M_{\boldsymbol{kpq}}+\sigma_{\boldsymbol{p}}M_{\boldsymbol{pqk}}+\sigma_{\boldsymbol{q}}M_{\boldsymbol{qkp}}=0; \tag{3}$$

this implies that the nonlinear terms of Eq. (2) conserve a total "generalized energy," defined as

$$E\doteq\tfrac{1}{2}\sum_{\boldsymbol{k}}\sigma_{\boldsymbol{k}}\langle|\psi_{\boldsymbol{k}}(t)|^2\rangle. \tag{4}$$

Here the angle brackets denote an ensemble average. For some problems (e.g., two-dimensional turbulence), Eq. (3) may be satisfied by more than one choice of $\sigma_{\boldsymbol{k}}$, each of which corresponds to a distinct nonlinear invariant.

A key statistical variable in our discussion of closures will be the *two-time correlation function* $C_{\boldsymbol{k}}(t,t')\doteq\langle\psi_{\boldsymbol{k}}(t)\psi^*_{\boldsymbol{k}}(t')\rangle$, which in stationary turbulence depends only on the difference of its time arguments: $C_{\boldsymbol{k}}(t,t')\doteq\mathcal{C}_{\boldsymbol{k}}(t-t')$. One can express the total energy in terms of the *equal-time correlation function* $C_{\boldsymbol{k}}(t)\doteq C_{\boldsymbol{k}}(t,t)$:

$$E=\tfrac{1}{2}\sum_{\boldsymbol{k}}\sigma_{\boldsymbol{k}}C_{\boldsymbol{k}}(t). \tag{5}$$

In addition, we define the *infinitesimal response function* (nonlinear Green's function) $R_{\boldsymbol{k}}(t,t')$ as the ensemble-averaged infinitesimal response to a source function $\bar{\eta}_{\boldsymbol{k}}(t)$ added to the right-hand side of Eq. (2):

$$R_{\boldsymbol{k}}(t,t')\doteq\left\langle\frac{\delta\psi_{\boldsymbol{k}}(t)}{\delta\bar{\eta}_{\boldsymbol{k}}(t')}\right\rangle\Big|_{\bar{\eta}_{\boldsymbol{k}}=0}. \tag{6}$$

The RMC for Eq. (2) follows from a Markovianization of the DIA response-function equation,

$$\partial_t R_{\boldsymbol{k}}(t,t')+\eta_{\boldsymbol{k}}(t)\,R_{\boldsymbol{k}}(t,t')=\delta(t-t'), \tag{7}$$

with $R_{\boldsymbol{k}}(t,-\infty)=0$, and an application of the fluctuation–dissipation (FD) ansatz[6,25]

$$C_{\boldsymbol{k}}(t,t')=C^{1/2}_{\boldsymbol{k}}(t)\,\bar{r}_{\boldsymbol{k}}(t,t')\,C^{1/2*}_{\boldsymbol{k}}(t') \tag{8}$$

to the two-time correlation functions that appear in the equal-time covariance equation. The quantity $\bar{r}_{\boldsymbol{k}}$ is related to the Markovianized nonlinear damping $\eta_{\boldsymbol{k}}$ by

$$\bar{r}_{\boldsymbol{k}}(t,t')\doteq\begin{cases}\exp\left(-\int_{t'}^{t}\mathcal{P}(\eta_{\boldsymbol{k}})(\bar{t})\,d\bar{t}\right) & \text{for } t\geq t',\\ \exp\left(-\int_{t}^{t'}\mathcal{P}(\eta_{\boldsymbol{k}})^*(\bar{t})\,d\bar{t}\right) & \text{for } t<t'.\end{cases} \tag{9}$$

Here $\mathcal{P}(\eta)\doteq\operatorname{Re}\eta\,\mathrm{H}(\operatorname{Re}\eta)+i\operatorname{Im}\eta$, where H is the Heaviside unit step function. The introduction of the $\mathcal{P}$ operator ensures that $\bar{r}_{\boldsymbol{k}}$ is positive-semidefinite for any value of $\eta_{\boldsymbol{k}}$ and that the $C_{\boldsymbol{k}}(t,t')$ determined from Eq. (8) remains bounded as $t-t'\to\infty$ [assuming that $C_{\boldsymbol{k}}(t)$ itself is bounded]. Note that the frequently used steady-state "single-pole" approximation

$$\mathcal{C}_{\boldsymbol{k}}(t-t')\approx\exp(-\eta_{\boldsymbol{k}}|t-t'|)\mathcal{C}_{\boldsymbol{k}}(0) \tag{10}$$

is a special case of Eq. (8).

The resulting equations for the RMC are[6]

$$\partial_t C_{\boldsymbol{k}}(t)+2\operatorname{Re}\eta_{\boldsymbol{k}}(t)\,C_{\boldsymbol{k}}(t)=2F_{\boldsymbol{k}}(t), \tag{11a}$$

$$\eta_{\boldsymbol{k}}\doteq\nu_{\boldsymbol{k}}-\sum_{\boldsymbol{k}+\boldsymbol{p}+\boldsymbol{q}=\boldsymbol{0}}M_{\boldsymbol{kpq}}M^*_{\boldsymbol{pqk}}\Theta^*_{\boldsymbol{pqk}}\,C^{1/2}_{\boldsymbol{q}}\,C^{-1/2}_{\boldsymbol{k}}, \tag{11b}$$

$$F_{\boldsymbol{k}}\doteq\tfrac{1}{2}\operatorname{Re}\sum_{\boldsymbol{k}+\boldsymbol{p}+\boldsymbol{q}=\boldsymbol{0}}|M_{\boldsymbol{kpq}}|^2\Theta_{\boldsymbol{kpq}}C^{1/2}_{\boldsymbol{p}}\,C^{1/2}_{\boldsymbol{q}}, \tag{11c}$$

$$\partial_t\Theta_{\boldsymbol{kpq}}+[\eta_{\boldsymbol{k}}+\mathcal{P}(\eta_{\boldsymbol{p}})+\mathcal{P}(\eta_{\boldsymbol{q}})]\Theta_{\boldsymbol{kpq}}=C^{1/2}_{\boldsymbol{p}}C^{1/2}_{\boldsymbol{q}}, \tag{11d}$$

$$\Theta_{\boldsymbol{kpq}}(0) = 0. \tag{11e}$$

In order for Eq. (11d) to have a steady-state solution, $\lim_{t\to\infty} \mathrm{Re}[\eta_{\boldsymbol{k}} + \mathcal{P}(\eta_{\boldsymbol{p}}) + \mathcal{P}(\eta_{\boldsymbol{q}})] > 0$; hence, $\lim_{t\to\infty} \Theta_{\boldsymbol{kpq}} \geq 0$ for all triads $\boldsymbol{k}, \boldsymbol{p}, \boldsymbol{q}$. From Eq. (11c) we then see that $F_{\boldsymbol{k}} \geq 0$, so that Eq. (11a) implies $\mathrm{Re}\,\eta_{\boldsymbol{k}} \geq 0$ in a steady state. This, in turn, ensures that Eq. (8) reduces in a steady state to the equilibrium FD Theorem,

$$C_{\boldsymbol{k}}(t,t') = R_{\boldsymbol{k}}(t,t')C_{\boldsymbol{k}}(\infty) \qquad (t > t'), \tag{12}$$

where $R_{\boldsymbol{k}}$ is the steady-state solution of Eq. (7).

The RMC has many desirable properties, such as the existence of an underlying Langevin representation and the conservation of the generalized energies (4) when $\nu_{\boldsymbol{k}} = 0$. However, because it is not invariant to random Galilean transformations, we are motivated to construct a related closure that additionally respects this property.

III. THE TEST-FIELD MODEL

In this section we demonstrate that the realizability of the TFM, like that of the EDQNM closure, is not guaranteed in the presence of linear waves (see Fig. 1). Let us first outline the construction of the TFM for Eq. (1). In the Navier–Stokes equation, Kraichnan observed that the rate at which advection couples the solenoidal and compressive components of a "test" velocity field $\boldsymbol{v}_{\boldsymbol{k}}$ in the absence of pressure can be taken as a measure of the interaction of an eddy with an advecting field.[9] He considered a modified Navier–Stokes system in which the solenoidal component $\boldsymbol{v}^S_{\boldsymbol{k}}$ of a "test" velocity field $\boldsymbol{v}_{\boldsymbol{k}}$ is distorted by advection of the compressive component $\boldsymbol{v}^C_{\boldsymbol{k}}$ (and *vice versa*). That is, in the nonlinearity, the cross terms that couple the solenoidal and compressive parts of the test field are removed. Upon applying the FD ansatz

$$C_{\boldsymbol{k}}(t,t') = R_{\boldsymbol{k}}(t,t')C_{\boldsymbol{k}}(t) \qquad (t > t') \tag{13}$$

and a subsequent Markovianization to the statistical equations for $\boldsymbol{v}^S_{\boldsymbol{k}}$ and $\boldsymbol{v}^C_{\boldsymbol{k}}$, Kraichnan obtained a (complex) nonlinear eddy-turnover rate, $\eta^{\mathrm{S}}_{\boldsymbol{k}}$, which he used in place of $\eta_{\boldsymbol{k}}$ in the expression for the DIA-based EDQNM triad interaction time. What results is a closure invariant to random Galilean transformations.[9,21]

Before proceeding, let us correct a typographical error in the original TFM paper. Equations (4.7) in Ref. 9 should read

$$\eta^S(k,t) = \pi k \int\!\!\int_\Delta b^G_{kpq}\Theta^G_{pqk}(t)U(q,t)\,pq\,dp\,dq, \tag{14a}$$

$$\eta^C(k,t) = 2\pi k \int\!\!\int_\Delta b^G_{kpq}\Theta^G_{pqk}(t)U(q,t)\,pq\,dp\,dq. \tag{14b}$$

The quantity Θ^G_{kpq} is in general symmetric only in its last two indices. An attempt to correct this error was made in a footnote of Ref. 21, but unfortunately the same erroneous equation was displayed there. Nevertheless, Eqs. (13) and (14) of Ref. 21 in two dimensions are consistent with our Eqs. (14); furthermore, Eqs. (2.17) and (2.18) of Ref. 10 are the correct generalizations of Eqs. (14) to inhomogeneous turbulence.

An early attempt to extend the TFM to dynamics involving oscillatory linear behavior was made by Holloway and Hendershott[30] in the context of Rossby-wave turbulence. However, these authors did not renormalize the linear frequency. They argued that only the real part of the damping enters the energy equation. Nevertheless, both the real and imaginary parts of the nonlinear damping should contribute to the evolution of the triad interaction time; this latter effect was ignored in their work.[31] Furthermore, it can be shown that the closure of Holloway and Hendershott (which incorporated the bare linear frequency in the expression for the triad interaction time) is guaranteed to predict a positive energy spectrum only in a steady state.[6,32]

In our notation, the underlying equations for the solenoidal and compressive components of the test field appear as

$$\left(\frac{\partial}{\partial t} + \nu_{\boldsymbol{k}}\right)\boldsymbol{v}^S_{\boldsymbol{k}}(t) = \boldsymbol{P}(\boldsymbol{k}) \sum_{\boldsymbol{k}+\boldsymbol{p}+\boldsymbol{q}=\boldsymbol{0}} M^U_{\boldsymbol{kpq}}\boldsymbol{v}^{C*}_{\boldsymbol{p}}(t)\hat{\psi}^*_{\boldsymbol{q}}(t), \tag{15a}$$

$$\left(\frac{\partial}{\partial t} + \nu_{\boldsymbol{k}}\right)\boldsymbol{v}^C_{\boldsymbol{k}}(t) = \boldsymbol{\Pi}(\boldsymbol{k}) \sum_{\boldsymbol{k}+\boldsymbol{p}+\boldsymbol{q}=\boldsymbol{0}} M^U_{\boldsymbol{kpq}}\boldsymbol{v}^{S*}_{\boldsymbol{p}}(t)\hat{\psi}^*_{\boldsymbol{q}}(t). \tag{15b}$$

Here $\boldsymbol{P}(\boldsymbol{k}) \doteq \boldsymbol{1} - \boldsymbol{\Pi}(\boldsymbol{k})$ is the projection tensor, where $\boldsymbol{\Pi}(\boldsymbol{k})$ is the tensor with components $\Pi_{ij} \doteq k_i k_j/k^2$, $\boldsymbol{v}^S_{\boldsymbol{k}} \doteq \boldsymbol{P}(\boldsymbol{k})\,\boldsymbol{v}_{\boldsymbol{k}}$, and $\boldsymbol{v}^C_{\boldsymbol{k}} \doteq \boldsymbol{\Pi}(\boldsymbol{k})\,\boldsymbol{v}_{\boldsymbol{k}}$. The advecting field $\hat{\psi}_{\boldsymbol{q}}$ is taken to have the correlation function of $\psi_{\boldsymbol{q}}$ and the response function of $\boldsymbol{v}^S_{\boldsymbol{k}}$.

The evolution of the nonlinear damping rates $\eta^{\mathrm{S}}_{\boldsymbol{k}}$ and $\eta^{\mathrm{C}}_{\boldsymbol{k}}$ for the fields $\boldsymbol{v}^S_{\boldsymbol{k}}$ and $\boldsymbol{v}^C_{\boldsymbol{k}}$ may be expressed in terms of the coefficient

$$B^G(k,p,q) \doteq M^{\mathrm{U}}_{\boldsymbol{kpq}}M^{\mathrm{U}}_{\boldsymbol{pkq}}\boldsymbol{P}(\boldsymbol{k}) : \boldsymbol{\Pi}(\boldsymbol{p}). \tag{16}$$

Since $\boldsymbol{P}(\boldsymbol{k}) : \boldsymbol{\Pi}(\boldsymbol{p}) = \boldsymbol{P}(\boldsymbol{p}) : \boldsymbol{\Pi}(\boldsymbol{k})$, it is convenient to define modified mode-coupling coefficients

$$M^{\mathrm{G}}_{\boldsymbol{kpq}} \doteq M^{\mathrm{U}}_{\boldsymbol{kpq}}[\boldsymbol{P}(\boldsymbol{k}) : \boldsymbol{\Pi}(\boldsymbol{p})]^{1/2} \tag{17}$$

such that $B^G(k,p,q) = M^{\mathrm{G}}_{\boldsymbol{kpq}}M^{\mathrm{G}}_{\boldsymbol{pkq}}$. In two dimensions, the tensor contraction $\boldsymbol{P}(\boldsymbol{k}) : \boldsymbol{\Pi}(\boldsymbol{p})$ evaluates to

$$\boldsymbol{P}(\boldsymbol{k}) : \boldsymbol{\Pi}(\boldsymbol{p}) = \frac{(\hat{\boldsymbol{z}}\cdot\boldsymbol{k}\times\boldsymbol{p})^2}{k^2p^2}. \tag{18}$$

The final test-field model equations are then

$$\partial_t C_{\boldsymbol{k}} + 2\,\mathrm{Re}\,\eta_{\boldsymbol{k}}\,C_{\boldsymbol{k}} = 2F_{\boldsymbol{k}}, \tag{19a}$$

$$\eta_{\boldsymbol{k}} \doteq \nu_{\boldsymbol{k}} - \sum_{\boldsymbol{k}+\boldsymbol{p}+\boldsymbol{q}=\boldsymbol{0}} M_{\boldsymbol{kpq}} M^*_{\boldsymbol{pqk}} \theta^*_{\boldsymbol{pqk}}\, C_{\boldsymbol{q}}, \tag{19b}$$

$$F_{\boldsymbol{k}} \doteq \tfrac{1}{2}\,\mathrm{Re} \sum_{\boldsymbol{k}+\boldsymbol{p}+\boldsymbol{q}=\boldsymbol{0}} |M_{\boldsymbol{kpq}}|^2 \theta_{\boldsymbol{kpq}} C_{\boldsymbol{p}}\, C_{\boldsymbol{q}}, \tag{19c}$$

$$\partial_t \theta_{\boldsymbol{kpq}} + \left(\eta^{\mathrm{S}}_{\boldsymbol{k}} + \eta^{\mathrm{S}}_{\boldsymbol{p}} + \eta^{\mathrm{S}}_{\boldsymbol{q}}\right) \theta_{\boldsymbol{kpq}} = 1, \quad \theta_{\boldsymbol{kpq}}(0) = 0, \tag{19d}$$

$$\eta^{\mathrm{S}}_{\boldsymbol{k}} \doteq \nu_{\boldsymbol{k}} + g \sum_{\boldsymbol{k}+\boldsymbol{p}+\boldsymbol{q}=\boldsymbol{0}} M^{\mathrm{G}}_{\boldsymbol{kpq}} M^{\mathrm{G}^*}_{\boldsymbol{pkq}} \theta^{\mathrm{G}^*}_{\boldsymbol{pqk}}\, C_{\boldsymbol{q}}, \tag{19e}$$

$$\eta^{\mathrm{C}}_{\boldsymbol{k}} \doteq \nu_{\boldsymbol{k}} + \lambda g \sum_{\boldsymbol{k}+\boldsymbol{p}+\boldsymbol{q}=\boldsymbol{0}} M^{\mathrm{G}}_{\boldsymbol{kpq}} M^{\mathrm{G}^*}_{\boldsymbol{pkq}} \theta^{\mathrm{G}^*}_{\boldsymbol{pqk}}\, C_{\boldsymbol{q}}, \tag{19f}$$

$$\partial_t \theta^{\mathrm{G}}_{\boldsymbol{kpq}} + \left(\eta^{\mathrm{C}}_{\boldsymbol{k}} + \eta^{\mathrm{S}}_{\boldsymbol{p}} + \eta^{\mathrm{S}}_{\boldsymbol{q}}\right) \theta^{\mathrm{G}}_{\boldsymbol{kpq}} = 1, \quad \theta^{\mathrm{G}}_{\boldsymbol{kpq}}(0) = 0. \tag{19g}$$

The value of the overall multiplicative factor g entering the expressions for $\eta^{\mathrm{S}}_{\boldsymbol{k}}$ and $\eta^{\mathrm{C}}_{\boldsymbol{k}}$ is arbitrarily taken in this work to be 1.0, in good agreement with the value 1.06 calculated by Kraichnan[9] in a comparison of the TFM with the DIA. This factor comes from a rescaling of the characteristic times for interplay between $\boldsymbol{v}^S_{\boldsymbol{k}}$ and $\boldsymbol{v}^C_{\boldsymbol{k}}$. The factor λ represents the number of solenoidal components associated with each compressive component: in two dimensions $\lambda = 1$, while in three dimensions $\lambda = 2$.

The addition of a uniform field to $\hat{\psi}_{\boldsymbol{q}}$ makes no contribution to the right-hand sides of Eqs. (15), since $\boldsymbol{P}(\boldsymbol{k})\boldsymbol{\Pi}(-\boldsymbol{k}) = \boldsymbol{\Pi}(\boldsymbol{k})\boldsymbol{P}(-\boldsymbol{k}) = 0$. Equations (19) are therefore invariant to random Galilean transformation. As Kraichnan pointed out, the small-wave-number contributions to the nonlinear damping coefficients $\eta^{\mathrm{S}}_{\boldsymbol{k}}$ and $\eta^{\mathrm{C}}_{\boldsymbol{k}}$ are proportional to the mean-square shear rather than to the kinetic energy.

The proof of realizability for both the TFM and the EDQNM is based on the reality of the renormalized damping for Navier–Stokes turbulence.[9] Unfortunately, with the inclusion of wave dynamics, the closure described by Eqs. (19) is not always realizable, just as is the case with the EDQNM. To illustrate, let us apply the TFM to the degenerate three-mode system that was used in Part I to establish the nonrealizability of the EDQNM,

$$\left(\partial_t + \tfrac{1}{2}i\omega - \tfrac{1}{2}\gamma\right)\psi_k(t) = M\psi^*_p\psi^*_q, \tag{20a}$$

$$\left(\partial_t + \tfrac{1}{2}i\omega - \tfrac{1}{2}\gamma\right)\psi_p(t) = -M\psi^*_q\psi^*_k, \tag{20b}$$

$$\partial_t \psi_q(t) = 0. \tag{20c}$$

For example, these interaction coefficients can be obtained by truncating the two-dimensional Navier–Stokes equations for the velocity field down to the single wavenumber triad[33,34]

$$k = \sqrt{2}M, \qquad p = \sqrt{2}M, \qquad q = 2M. \tag{21}$$

Let us adopt the normalization $\psi_{\boldsymbol{k}} = k\bar{\psi}_{\boldsymbol{k}}$, where $\bar{\psi}_{\boldsymbol{k}}$ is the stream function. The unsymmetrized mode-coupling coefficient is given by

$$M^{\mathrm{U}}_{\boldsymbol{kpq}} = \frac{-p^2}{kpq}(\hat{\boldsymbol{z}}\cdot\boldsymbol{p}\times\boldsymbol{q}). \tag{22}$$

Hence

$$M_{\boldsymbol{kpq}} = \frac{(q^2 - p^2)}{kpq}(\hat{\boldsymbol{z}}\cdot\boldsymbol{p}\times\boldsymbol{q}), \tag{23a}$$

and for contributing triads (to within an arbitrary sign)

$$M^{\mathrm{G}}_{\boldsymbol{kpq}} = \frac{1}{kpq}|\hat{\boldsymbol{z}}\cdot\boldsymbol{p}\times\boldsymbol{q}|^2, \tag{23b}$$

consistent with the expressions (15) and (16) in Ref. 21 for $B_2(k,p,q) \doteq -M_{\boldsymbol{kpq}}M_{\boldsymbol{pqk}}$ and $B^G(k,p,q)$. For the selected triad, one finds upon noting

$$|\hat{\boldsymbol{z}}\cdot\boldsymbol{p}\times\boldsymbol{q}|^2 = \frac{1}{4}(k+p+q) \times(p+q-k)(q+k-p)(k+p-q) \tag{24}$$

that

$$M_{\boldsymbol{kpq}} = M, \qquad M_{\boldsymbol{pqk}} = -M, \qquad M_{\boldsymbol{qkp}} = 0, \tag{25a}$$

and

$$M^{\mathrm{G}}_{\boldsymbol{kpq}} = M^{\mathrm{G}}_{\boldsymbol{kqp}} = M^{\mathrm{G}}_{\boldsymbol{pqk}} = M^{\mathrm{G}}_{\boldsymbol{pkq}} = M^{\mathrm{G}}_{\boldsymbol{qkp}} = M^{\mathrm{G}}_{\boldsymbol{qpk}} = M. \tag{25b}$$

The TFM for (20) is thus

$$\partial_t C_k - \gamma C_k + 2M^2\,\mathrm{Re}\,\theta\, C_q C_k = 2M^2\,\mathrm{Re}\,\theta\, C_p C_q, \tag{26a}$$

$$\partial_t C_p - \gamma C_p + 2M^2\,\mathrm{Re}\,\theta\, C_q C_p = 2M^2\,\mathrm{Re}\,\theta\, C_k C_q, \tag{26b}$$

$$\partial_t C_q = 0, \tag{26c}$$

$$\partial_t \theta + \eta^S \theta = 1, \tag{26d}$$

$$\eta^S = -\gamma + i\omega + 2M^2\theta^*(C_k + C_p + C_q). \tag{26e}$$

Let us set $C_q(0) = 1$, so that $C_q(t) = 1$ for all t. Note that

$$\partial_t(C_k + C_p) = \gamma(C_k + C_p), \tag{27}$$

so that $E(t) \doteq \frac{1}{2}[C_k(t) + C_p(t)] = E_0 e^{\gamma t}$, with $E_0 \doteq \frac{1}{2}[C_k(0) + C_p(0)] > 0$.

In the limit where

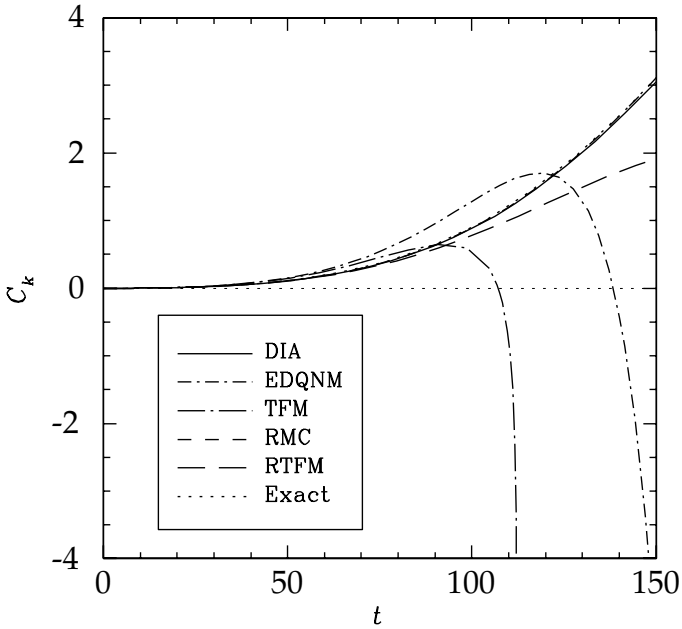

FIG. 1. Demonstration of the nonrealizability of the TFM in the presence of wave phenomena. The exact, DIA, and RMC solutions nearly coincide.

$$\epsilon \doteq \frac{M^2|\theta|[2E_0\exp(\gamma t)+1]}{\gamma} \ll 1, \tag{28}$$

we obtain for the case $C_k(0)=0$ the analytical solution found in Part I:

$$\begin{aligned} C_k(\pi/\gamma) &= E_0 e^{\pi}\{1-\exp\left(2M^2[\pi+\mathrm{O}(\epsilon)]\right)\} \\ &< 0 \qquad (\epsilon \ll 1). \end{aligned} \tag{29}$$

We verify *a posteriori* that $\epsilon \ll 1$ at the value $t=\pi/\gamma$, for sufficiently small M. In Fig. 1 we graph the numerical solution of the TFM for the parameters $\gamma = 0.02$, $M = 0.003$, and $E_0 = 1$. (Actually, for this value of M, the approximation $\epsilon \ll 1$ does not hold; nevertheless, the numerical solution in this case still turns out to be nonrealizable. While smaller values of M satisfying $\epsilon \ll 1$ lead to qualitatively similar results, the larger value used in Fig. 1 makes the nonrealizability more clearly visible.)

Some discussion has already appeared in the literature regarding the application of the TFM to anisotropic turbulence. In Ref. 35, Herring states that the TFM equations "for anisotropic, 2D turbulence are a simple extension of the corresponding formulas for the isotropic case; to retrieve the latter, one simply suppresses the ϕ-dependence of $U(\boldsymbol{k})$ and $g(\boldsymbol{k})$." Nevertheless, because Markovian closures were originally constructed for isotropic turbulence, it is conceivable that for anisotropic applications there may exist more general formulations.[36] The TFM has also been generalized and applied to isotropic passive scalar advection,[37–40] where more than one arbitrary constant enters the formalism. However, since the principal focus of this paper is on realizability and not anisotropy (or passive scalar advection), we will confine our attention to the development of a realizable version of Eqs. (19).

IV. THE REALIZABLE TEST-FIELD MODEL

Having established the nonrealizability of the TFM, we now present a modification, based on the FD ansatz (8), that will restore realizability to this random-Galilean-invariant closure. One may readily verify that Eqs. (19 a–d) follow from the time derivative of

$$C_{\boldsymbol{k}}(t,t) = \int_{-\infty}^{\infty} d\bar{t} \int_{-\infty}^{\infty} d\bar{\bar{t}}\, R_{\boldsymbol{k}}(t,\bar{t})\, \mathcal{F}_{\boldsymbol{k}}(\bar{t},\bar{\bar{t}})\, R^*_{\boldsymbol{k}}(t,\bar{\bar{t}}), \tag{30}$$

with $R_{\boldsymbol{k}}$ given by Eq. (7) and where

$$\mathcal{F}_{\boldsymbol{k}}(t,\bar{t}) = \mathcal{F}^{\mathrm{S}}_{\boldsymbol{k}}(t,\bar{t})\, r^{\mathrm{S}*}_{\boldsymbol{k}}(t,\bar{t})/r^*_{\boldsymbol{k}}(t,\bar{t}), \tag{31}$$

$$\begin{aligned} \mathcal{F}^{\mathrm{S}}_{\boldsymbol{k}}(t,\bar{t}) = \tfrac{1}{2} \sum_{\boldsymbol{k}+\boldsymbol{p}+\boldsymbol{q}=\boldsymbol{0}} |M_{\boldsymbol{kpq}}|^2 \\ \times C_{\boldsymbol{p}}(t)\, r^{\mathrm{S}^*}_{\boldsymbol{p}}(t,\bar{t})\, C_{\boldsymbol{q}}(t)\, r^{\mathrm{S}^*}_{\boldsymbol{q}}(t,\bar{t}), \end{aligned} \tag{32}$$

$$r_{\boldsymbol{k}}(t,t') \doteq \begin{cases} \exp\left(-\int_{t'}^{t} \eta_{\boldsymbol{k}}(\bar{t})\, d\bar{t}\right) & \text{for } t \geq t', \\ \exp\left(-\int_{t}^{t'} \eta^*_{\boldsymbol{k}}(\bar{t})\, d\bar{t}\right) & \text{for } t < t', \end{cases} \tag{33}$$

and

$$r^{\mathrm{S}}_{\boldsymbol{k}}(t,t') \doteq \begin{cases} \exp\left(-\int_{t'}^{t} \eta^{\mathrm{S}}_{\boldsymbol{k}}(\bar{t})\, d\bar{t}\right) & \text{for } t \geq t', \\ \exp\left(-\int_{t}^{t'} \eta^{\mathrm{S}*}_{\boldsymbol{k}}(\bar{t})\, d\bar{t}\right) & \text{for } t < t'. \end{cases} \tag{34}$$

The choice of $\mathcal{F}_{\boldsymbol{k}}$ given by Eq. (31) is not manifestly positive-semidefinite (e.g., see Appendix C of Part I); moreover, we have seen that it can lead to nonrealizable behavior. This is a consequence of an improper nonequilibrium FD ansatz, as was discussed in Part I.

Guided by the derivation of the RMC, we attempt to enforce realizability by replacing the ansatz (13) with the modified FD ansatz

$$C_{\boldsymbol{k}}(t,t') = C^{1/2}_{\boldsymbol{k}}(t)\, \bar{r}^{\mathrm{S}}_{\boldsymbol{k}}(t,t')\, C^{1/2*}_{\boldsymbol{k}}(t'), \tag{35}$$

where

$$\bar{r}^{\mathrm{S}}_{\boldsymbol{k}}(t,t') \doteq \begin{cases} \exp\left(-\int_{t'}^{t} \mathcal{P}(\eta^{\mathrm{S}}_{\boldsymbol{k}})(\bar{t})\, d\bar{t}\right) & \text{for } t \geq t', \\ \exp\left(-\int_{t}^{t'} \mathcal{P}(\eta^{\mathrm{S}}_{\boldsymbol{k}})^*(\bar{t})\, d\bar{t}\right) & \text{for } t < t'. \end{cases} \tag{36}$$

This leads to the expression

$$\begin{aligned} \mathcal{F}^{\mathrm{S}}_{\boldsymbol{k}}(t,\bar{t}) = \tfrac{1}{2} \sum_{\boldsymbol{k}+\boldsymbol{p}+\boldsymbol{q}=\boldsymbol{0}} |M_{\boldsymbol{kpq}}|^2 \\ \times C^{1/2*}_{\boldsymbol{p}}(t)\, \bar{r}^{\mathrm{S}^*}_{\boldsymbol{p}}(t,\bar{t})\, C^{1/2}_{\boldsymbol{p}}(\bar{t}) \\ \times C^{1/2*}_{\boldsymbol{q}}(t)\, \bar{r}^{\mathrm{S}^*}_{\boldsymbol{q}}(t,\bar{t})\, C^{1/2}_{\boldsymbol{q}}(\bar{t}), \end{aligned} \tag{37}$$

which, upon employing Theorems 1 and 2 of Part I, is seen to be positive-semidefinite. However, the additional factor of $r^{\mathrm{S}}_{\boldsymbol{k}}(t,\bar{t})/r_{\boldsymbol{k}}(t,\bar{t})$ appearing in Eq. (31) slightly complicates the situation. To ensure that $\mathcal{F}_{\boldsymbol{k}}$ itself is positive-semidefinite, we replace (31) with

$$\mathcal{F}_{\boldsymbol{k}}(t,\bar{t}) = \mathcal{F}^{\mathrm{S}}_{\boldsymbol{k}}(t,\bar{t})\,\hat{r}^{*}_{\boldsymbol{k}}(t,\bar{t}), \tag{38}$$

where $\mathcal{F}^{\mathrm{S}}_{\boldsymbol{k}}(t,\bar{t})$ is given by Eq. (37) and

$$\hat{r}_{\boldsymbol{k}}(t,t') \doteq \begin{cases} \exp\left(-\int_{t'}^{t} \mathcal{P}[\eta^{\mathrm{S}}_{\boldsymbol{k}}(\bar{t}) - \eta_{\boldsymbol{k}}(\bar{t})]\,d\bar{t}\right) & \text{for } t \geq t', \\ \exp\left(-\int_{t}^{t'} \mathcal{P}[\eta^{\mathrm{S}}_{\boldsymbol{k}}(\bar{t}) - \eta_{\boldsymbol{k}}(\bar{t})]^{*}\,d\bar{t}\right) & \text{for } t < t'. \end{cases} \tag{39}$$

Upon inserting Eqs. (38) and (37) into Eq. (30), one finds that $C_{\boldsymbol{k}}(t)$ remains real and non-negative, provided that the initial condition is non-negative. Differentiation of this expression for $C_{\boldsymbol{k}}(t)$ with respect to t leads to the realizable test-field model (RTFM) equations:

$$\partial_t C_{\boldsymbol{k}} + 2\,\mathrm{Re}\,\eta_{\boldsymbol{k}}\,C_{\boldsymbol{k}} = 2F_{\boldsymbol{k}}, \tag{40a}$$

$$\eta_{\boldsymbol{k}} \doteq \nu_{\boldsymbol{k}} - \sum_{\boldsymbol{k}+\boldsymbol{p}+\boldsymbol{q}=\boldsymbol{0}} M_{\boldsymbol{kpq}} M^{*}_{\boldsymbol{pqk}} \Theta^{*}_{\boldsymbol{pqk}}\, C_{\boldsymbol{q}}^{1/2}\, C_{\boldsymbol{k}}^{-1/2}, \tag{40b}$$

$$F_{\boldsymbol{k}} \doteq \tfrac{1}{2}\,\mathrm{Re} \sum_{\boldsymbol{k}+\boldsymbol{p}+\boldsymbol{q}=\boldsymbol{0}} |M_{\boldsymbol{kpq}}|^2 \Theta_{\boldsymbol{kpq}} C_{\boldsymbol{p}}^{1/2}\, C_{\boldsymbol{q}}^{1/2}, \tag{40c}$$

$$\begin{aligned} \partial_t \Theta_{\boldsymbol{kpq}} + \left[\mathcal{P}(\eta^{\mathrm{S}}_{\boldsymbol{k}} - \eta_{\boldsymbol{k}}) + \eta_{\boldsymbol{k}} + \mathcal{P}(\eta^{\mathrm{S}}_{\boldsymbol{p}}) + \mathcal{P}(\eta^{\mathrm{S}}_{\boldsymbol{q}})\right]\Theta_{\boldsymbol{kpq}} \\ = C_{\boldsymbol{p}}^{1/2} C_{\boldsymbol{q}}^{1/2}, \qquad \Theta_{\boldsymbol{kpq}}(0) = 0, \end{aligned} \tag{40d}$$

$$\eta^{\mathrm{S}}_{\boldsymbol{k}} \doteq \nu_{\boldsymbol{k}} + g \sum_{\boldsymbol{k}+\boldsymbol{p}+\boldsymbol{q}=\boldsymbol{0}} M^{\mathrm{G}}_{\boldsymbol{kpq}} M^{\mathrm{G}^{*}}_{\boldsymbol{pkq}} \Theta^{\mathrm{G}^{*}}_{\boldsymbol{pqk}}\, C_{\boldsymbol{q}}^{1/2}\, C_{\boldsymbol{k}}^{-1/2}, \tag{40e}$$

$$\eta^{\mathrm{C}}_{\boldsymbol{k}} \doteq \nu_{\boldsymbol{k}} + g\lambda \sum_{\boldsymbol{k}+\boldsymbol{p}+\boldsymbol{q}=\boldsymbol{0}} M^{\mathrm{G}}_{\boldsymbol{kpq}} M^{\mathrm{G}^{*}}_{\boldsymbol{pkq}} \Theta^{\mathrm{G}^{*}}_{\boldsymbol{pqk}}\, C_{\boldsymbol{q}}^{1/2}\, C_{\boldsymbol{k}}^{-1/2}, \tag{40f}$$

$$\begin{aligned} \partial_t \Theta^{\mathrm{S}}_{\boldsymbol{kpq}} + \left[\eta^{\mathrm{C}}_{\boldsymbol{k}} + \mathcal{P}(\eta^{\mathrm{S}}_{\boldsymbol{p}}) + \mathcal{P}(\eta^{\mathrm{S}}_{\boldsymbol{q}})\right]\Theta^{\mathrm{S}}_{\boldsymbol{kpq}} = C_{\boldsymbol{p}}^{1/2} C_{\boldsymbol{q}}^{1/2}, \\ \Theta^{\mathrm{S}}_{\boldsymbol{kpq}}(0) = 0. \end{aligned} \tag{40g}$$

These equations typically yield $\lim_{t\to\infty}(\eta^{\mathrm{S}}_{\boldsymbol{k}} - \eta_{\boldsymbol{k}}) \geq 0$, in which case the steady-state forms of the RTFM and the TFM, Eqs. (19), agree. The restriction $\eta^{\mathrm{S}}_{\boldsymbol{k}} \geq \eta_{\boldsymbol{k}}$ is simply the condition that guarantees that the steady-state covariance predicted by the TFM,

$$\int_{-\infty}^{\infty} d\bar{t} \int_{-\infty}^{\infty} d\bar{\bar{t}}\, R_{\boldsymbol{k}}(\infty,\bar{t})\, \mathcal{F}_{\boldsymbol{k}}(\bar{t},\bar{\bar{t}})\, R^{*}_{\boldsymbol{k}}(\infty,\bar{\bar{t}}), \tag{41}$$

with $\mathcal{F}_{\boldsymbol{k}}$ given by Eqs. (31) and (32), is non-negative.

The argument used to prove the existence of an underlying amplitude equation for the RMC in Part I (see also Ref. 27) may be used to establish an underlying Langevin equation for the RTFM:

$$\partial_t \psi_{\boldsymbol{k}}(t) + \eta_{\boldsymbol{k}}(t)\,\psi_{\boldsymbol{k}}(t) = f_{\boldsymbol{k}}(t). \tag{42}$$

Unlike in the corresponding representation of the TFM, no assumption of δ-correlated statistics is placed on the noise term f; for this reason, the RTFM is in general expected to exhibit improved transient behavior, even in the absence of linear waves.

The realizability of the RTFM for the degenerate system of three interacting waves is evident in Fig. 1: we see that, unlike the TFM and EDQNM, the RTFM predicts non-negative energies. Significant discrepancy relative to the exact, DIA, and RMC solutions is observed in the RTFM solution; this is presumably a result of the heuristic construction of test-field models.

By following the construction of the multiple-field RMC equations, one may in principle construct equations for a multiple-field realizable test-field model. This would provide an alternative to the multiple-field TFM described by Kraichnan[10] that has the advantages of realizability in the presence of a linear wave term. Even in the absence of wave phenomena, this multiple-field RTFM would conserve all quadratically nonlinear invariants, in contrast to Kraichnan's inhomogeneous test-field model, which can only conserve a set of such invariants for which the corresponding $\boldsymbol{\sigma}$ matrices are simultaneously diagonalizable.[25]

In two dimensions, there is no distinction between the compressive and solenoidal damping rates: $\eta^{\mathrm{S}}_{\boldsymbol{k}} = \eta^{\mathrm{C}}_{\boldsymbol{k}}$. A computational savings in Eqs. (40) can then be exploited: whenever $\mathrm{Re}\,\eta^{\mathrm{S}}_{\boldsymbol{k}}(\bar{t}) \geq \mathrm{Re}\,\eta_{\boldsymbol{k}}(\bar{t})$ for all $\bar{t} \leq t$, it follows that $\Theta_{\boldsymbol{kpq}}(t) = \Theta^{\mathrm{S}}_{\boldsymbol{kpq}}(t)$.

V. ANISOTROPIC BIN AVERAGING

In this section, we briefly discuss the generalization of the bin-averaging algorithm developed in Ref. 22 to anisotropic dynamics. This method exploits the smoothness of the statistical variables in wave-number space (a property not afforded by the primitive dynamics) and requires the computation of the integral

$$\begin{aligned} \int_{k_<}^{k_>} k\,dk \int_{\alpha_<}^{\alpha_>} d\alpha \int_{p_<}^{p_>} p\,dp \int_{\beta_<}^{\beta_>} d\beta \int_{q_<}^{q_>} q\,dq \int_{\gamma_<}^{\gamma_>} d\gamma \\ \times \delta(\boldsymbol{k}+\boldsymbol{p}+\boldsymbol{q})\, f(\boldsymbol{k},\boldsymbol{p},\boldsymbol{q}), \end{aligned} \tag{43}$$

where α, β, and γ specify the directions of the vectors $\boldsymbol{k}$, $\boldsymbol{p}$, and $\boldsymbol{q}$ respectively. Referring to the 3×8 (radial $\times$ angular) bin geometry in Fig. 2, one observes that this integral represents the product, weighted by the function f, of the areas of bins P and Q that interact to affect modes lying in bin K. The reduction of this problem from

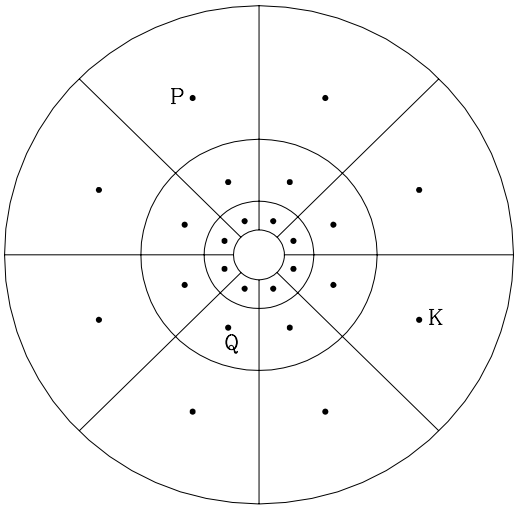

FIG. 2. Anisotropic bin geometry.

a six-dimensional integral to a three-dimensional numerical integration is described in Appendix A.

The algorithm we have developed has been subjected to exhaustive tests, including comparison with known analytical solutions for several anisotropic special cases. In addition, certain nontrivial consistency properties were checked. For example, the summation theorem for integrals was verified for thousands of random subdivisions of the partitions to ensure that no small structures in the highly discontinuous integrand were being ignored. In the next two sections, we use this anisotropic bin-averaging scheme, in the presence of many interacting modes, to obtain statistical-closure solutions of the Hasegawa–Mima equation.

VI. SHORT-WAVELENGTH HASEGAWA–MIMA EQUATION

Although the anisotropic drift-wave frequency in the Hasegawa–Mima equation will not directly affect the evolution of the energy spectrum, it can introduce a frequency mismatch (and anisotropy) into the expression for the triad interaction time, which in turn will affect the evolution of the energy spectrum. In the normalization $\psi_{\boldsymbol{k}} = k\bar{\psi}_{\boldsymbol{k}}$, where $\bar{\psi}_{\boldsymbol{k}}$ is the stream function, the scale-invariant mode-coupling coefficients for the short-wavelength ($k \geq 1$) Hasegawa–Mima equation are given in Eqs. (23a). The restriction to short wavelengths simplifies the analysis of the inertial-range scaling and allows one to make contact with Rossby-wave turbulence (in the absence of a free surface).[41]

We adopt the linear coefficient

$$\nu_{\boldsymbol{k}} = ik_y/k^2 + \gamma_{\boldsymbol{k}}, \tag{44}$$

where the first term arises from the diamagnetic drift frequency and the effects of short- and long-wavelength damping and of non-adiabatic forcing are modeled by the isotropic growth rate

$$\gamma_{\boldsymbol{k}} \doteq -D_1 k^8 - D_2 k^{-4} + \frac{\gamma_f}{\Delta_f} \begin{cases} 1 & \text{if } |k - k_f| < \frac{1}{2}\Delta_f, \\ 0 & \text{otherwise.} \end{cases} \tag{45}$$

As is common practice in numerical simulations of turbulence, hyperviscosities are introduced to reduce the extent of the active dissipation ranges. We model the wave-number range between $k = 1$ and $k = 59$ and choose

$$D_1 = 10^{-13}, \quad D_2 = 0.05, \tag{46a}$$

$$k_f = 4.212, \quad \Delta_f = 1.088, \quad \gamma_f = 0.0625. \tag{46b}$$

These parameters are identical to those used previously in Ref. 42. They were chosen such that the injection range occupies exactly two radial divisions when the wave numbers, treated as a continuum, are partitioned into 32 radial × 6 angular bins. This ensures that the forcing term in Eq. (45) is treated exactly by the wave-number partitioning scheme.

We exploit the reality condition $\psi_{\boldsymbol{k}} = \psi^*_{-\boldsymbol{k}}$, so that only 32×3 bins need to be explicitly evolved. To avoid any redundancy in the mode assignments arising from the additional symmetry $k_x \to -k_x$ (for fixed k_y) of the growth rate, we align the bin boundaries at $\theta = -\pi/2$, where θ represents the angular component of $\boldsymbol{k}$. The bin centers are then located at $\theta = -2\pi/3$, $\theta = 0$, and $\theta = 2\pi/3$. The linear growth rate and frequency are plotted in Figs. 3 and 4. The symbols indicate the bin-averaged values of the growth rate and frequency; the displacement of these values from the continuous curves results from the variation of these quantities over a bin.

A. Comparison of closure *vs.* numerical simulation

The closures were evolved from a statistical-equilibrium energy spectrum,

$$E(k) = \frac{1}{(2\pi)^2} \frac{\pi k}{1 + k^2}, \tag{47}$$

until a steady state was achieved.

In Fig. 5 we compare the steady-state energy spectra (averaged over wave-number angle) predicted by the RTFM and RMC with the time-averaged spectrum obtained from a direct numerical simulation with a resolution of 85×85 dealiased modes (128×128 total modes). The discreteness of the DNS solution in wave-number space, coupled with the anisotropy of the diamagnetic term, is responsible for the jagged behavior at the largest scales; the time average was sufficiently long to remove any temporal noise.

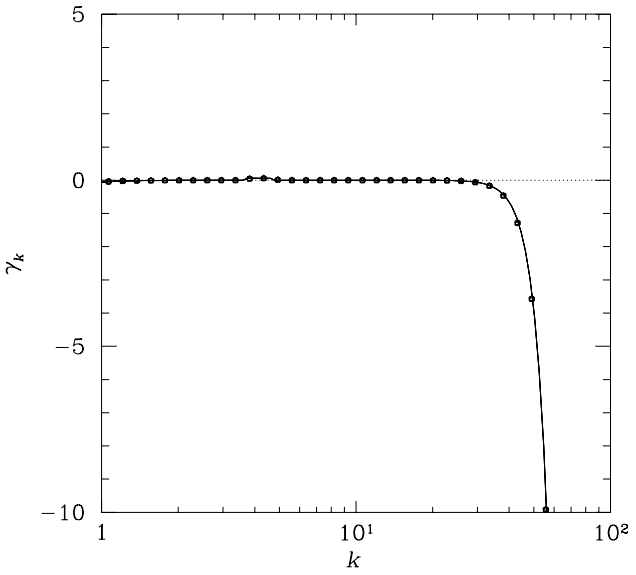

FIG. 3. Linear growth rate defined in Eq. (45).

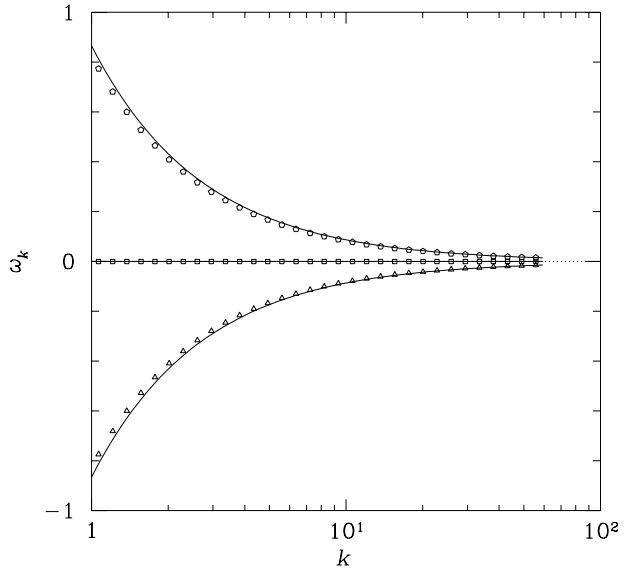

FIG. 4. Frequency $k_y V_{\rm d}/k^2$ used in the short-wavelength Hasegawa–Mima problem.

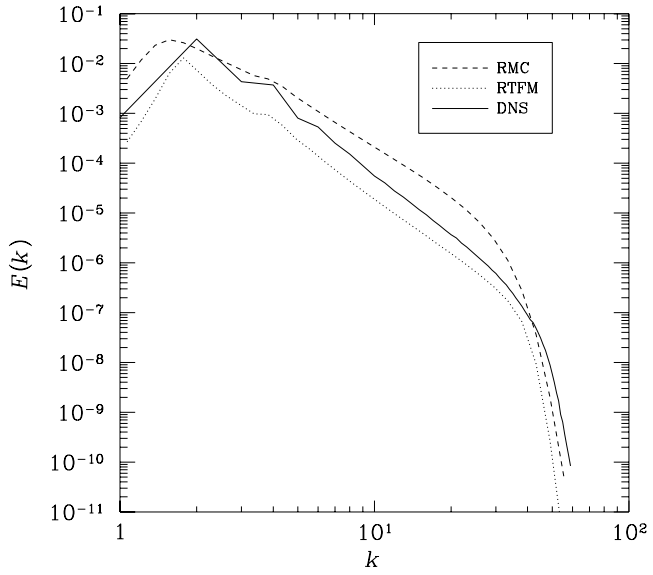

FIG. 5. Comparison of the steady-state energy spectra predicted by the RTFM, RMC, and conventional numerical simulation.

We see that the shape of the RTFM spectrum in the enstrophy inertial range is in rough agreement with the direct numerical simulation result, although the absolute energy level is lower. In contrast, the slope of the RMC is noticeably shallower. To emphasize this difference, we evaluate the logarithmic slopes of the energy spectra numerically in Figure 6. In the enstrophy range, the slope predicted by the RTFM closure takes on a maximum value of -3.6, to be compared with the slope of roughly -3.8 obtained for the DNS solution. The RMC, on the other hand, predicts a maximum slope of -3.2; this higher value results from the spurious energy transfer from large scales to small scales associated with the violation of random Galilean invariance. The discrepancy between these results and the Kolmogorov scaling of -3 is due in part to the fact that the enstrophy range is not well developed: the dissipation wave number $k_d \approx 40$ is only a factor of 8 larger than the maximum injection wave number. Better illustrations of high-resolution closure solutions for the enstrophy and energy inertial ranges of isotropic two-dimensional turbulence can be found in Refs. 22 and 24.

The dual cascade is clearly evident in the graphs of the energy and enstrophy transfers, Figs. 7 and 8. Note that there is significant enstrophy transfer to the long wavelengths, although the dominant transfer is still to the small scales. These graphs of the transfer function are useful for diagnosing the proximity of a solution to a steady state, where the nonlinear and linear contributions to the transfer must agree.

One expects the role of the diamagnetic velocity $V_{\rm d}$ to be relatively small for this case since the wave numbers are all larger than unity. Indeed, anisotropy en-

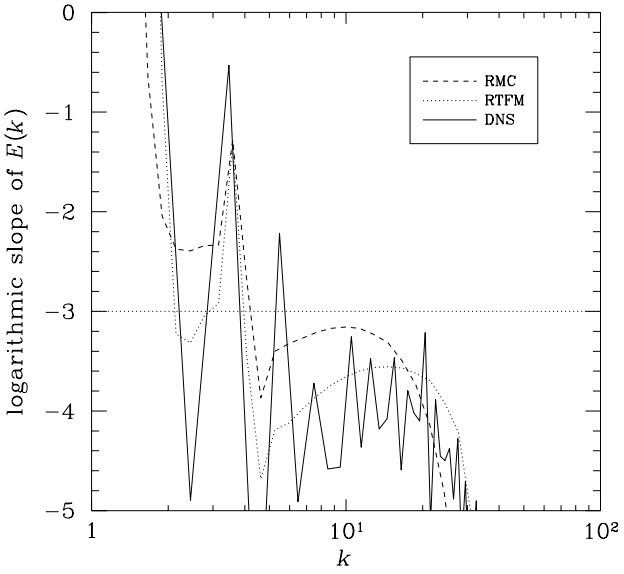

FIG. 6. Logarithmic slopes of the RMC and RTFM energy spectra in Fig. 5.

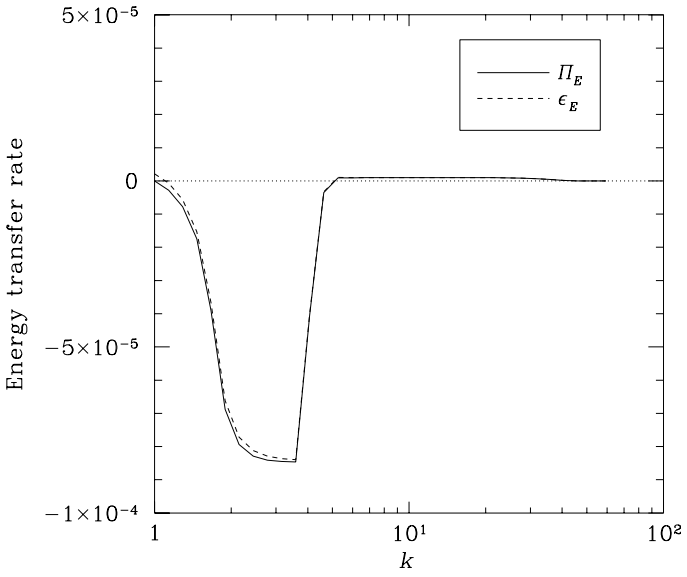

FIG. 7. Energy transfer for the RTFM solution in Fig. 5.

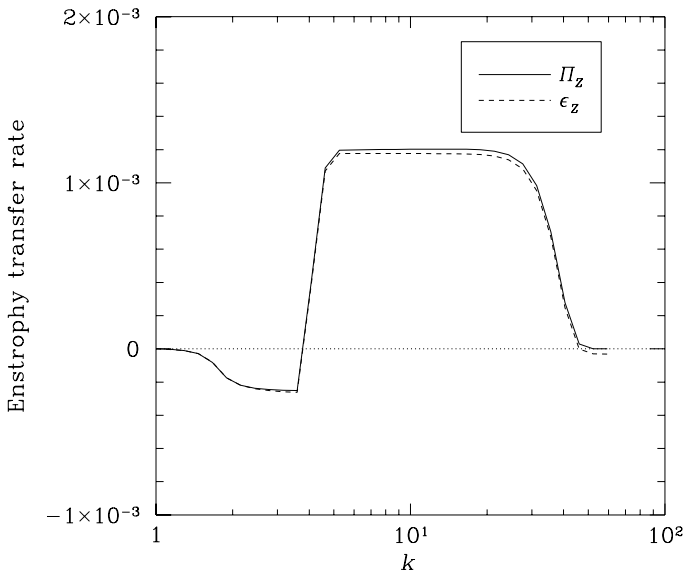

FIG. 8. Enstrophy transfer for the RTFM solution in Fig. 5.

ters only at the longest wavelengths, as is readily apparent from the angular standard deviation in Fig. 9 of the spectrum normalized to the mean energy in each wavenumber shell.

In Fig. 10 we illustrate that the removal of the anisotropic diamagnetic term ik_y/k^2 from Eq. (44) causes the RTFM fluctuation level to drop slightly at the longest wavelengths, but has no discernible effect in the inertial and dissipation ranges.

We verify the convergence of the wave-number partitioning scheme for the RMC solution in Fig. 11. Varying either the number of radial divisions or the number of angular divisions had no noticeable effect on the energy spectrum.

Finally, we mention a few computation statistics. For the RTFM, 108 852 distinct triads were evolved a total of 10 000 time steps (using the adaptive time-stepping mechanism discussed in Appendix B); saturation was achieved at $t = 2500$. This required 4.6 hours of CPU time on a Sun Ultra-1 SparcStation (the wave-number averaging required only 79 CPU seconds). In comparison, the numerical simulation required about 4 hours on a CRAY J90. For the RMC, the same computation evolved 101 175 distinct triads and required only 0.85 CPU hours. In this case, saturation occurred much earlier, at $t = 500$.

B. Two-time statistics

By initializing the DIA with the steady-state spectrum found using the RMC closure with 16×8 bins, we were able to evolve the DIA 200 time steps, or a time interval of 20. It was found that the energy spectrum had evolved slightly away from the RMC solution at the

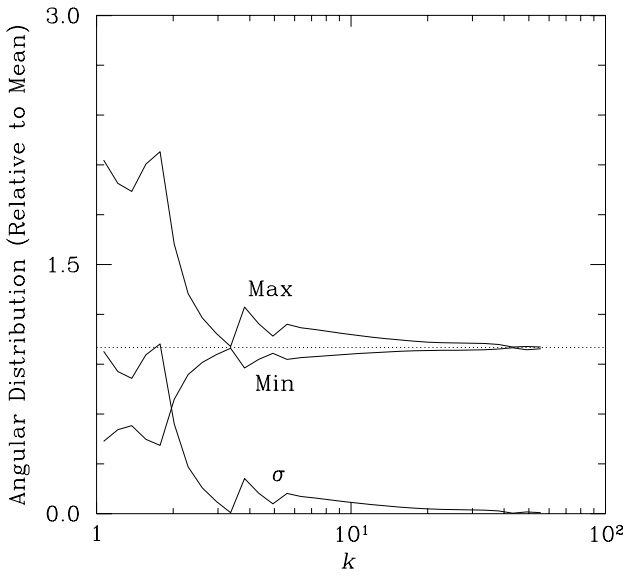

FIG. 9. Anisotropy of the RTFM energy spectrum of Fig. 5.

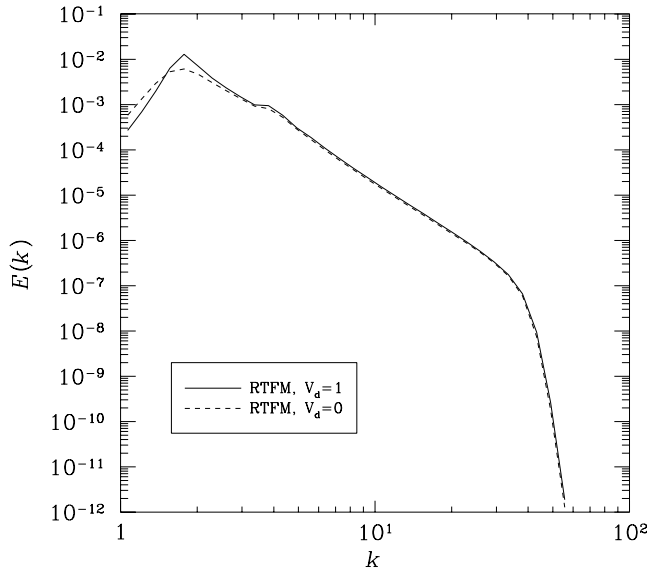

FIG. 10. Comparison of the anisotropic and isotropic RTFM predictions.

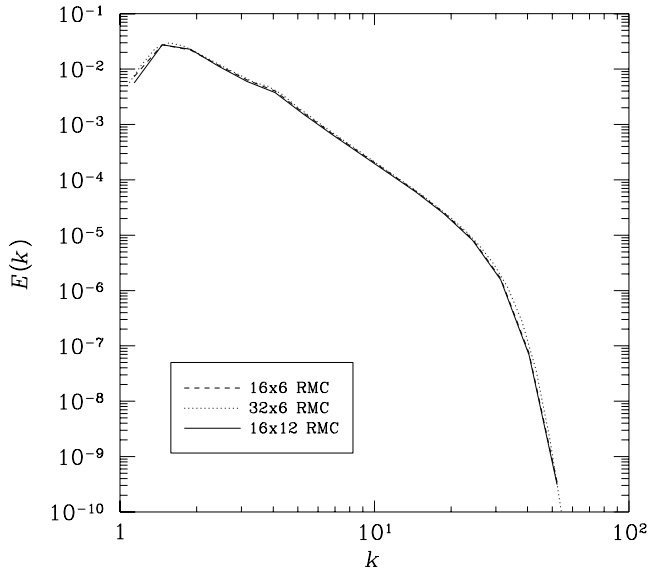

FIG. 11. Convergence of the wave-number partition for the RMC solution in Fig. 5.

smallest scales. At this time some of the modes were clearly still evolving; we therefore began a second DIA run initialized with the final energies from the first DIA run.[43] After 300 iterations, or a time interval of 30, there was no discernible change in the energy spectrum; however, it is not certain that the system had yet achieved a true steady state. This second run required 1.7 hours on a Sun Ultra-1 SparcStation.[44] The computational advantages of a Markovian closure like the RMC over the DIA are made very clear by this example: the final time step required 55 CPU seconds and the total computation time appeared to be increasing as the square of the number of time steps, as one expects for a system with many modes.[45] Nevertheless, it is interesting to examine typical two-time correlation and response function data, as depicted in Figs. 12 and 13. Note that the FD relation is well satisfied by these statistical quantities.

VII. HASEGAWA–MIMA EQUATION

Let us now consider the complete Hasegawa–Mima equation,

$$(1+k^2)\frac{\partial \Phi_{\boldsymbol{k}}}{\partial t} = -ik_y V_{\rm d}\Phi_{\boldsymbol{k}} + (1+k^2)\gamma_k \Phi_{\boldsymbol{k}} + \tfrac{1}{2}\sum_{\boldsymbol{k}+\boldsymbol{p}+\boldsymbol{q}=0} (q^2-p^2)(\hat{\boldsymbol{z}}\cdot\boldsymbol{p}\times\boldsymbol{q})\Phi^*_{\boldsymbol{p}}\Phi^*_{\boldsymbol{q}}, \tag{48}$$

and adopt the growth-rate function γ_k used by Waltz,[46]

$$\gamma_k = 0.06\left[1 - 0.5\left(\frac{|k_x|-0.5}{0.5}\right)^2\right.$$

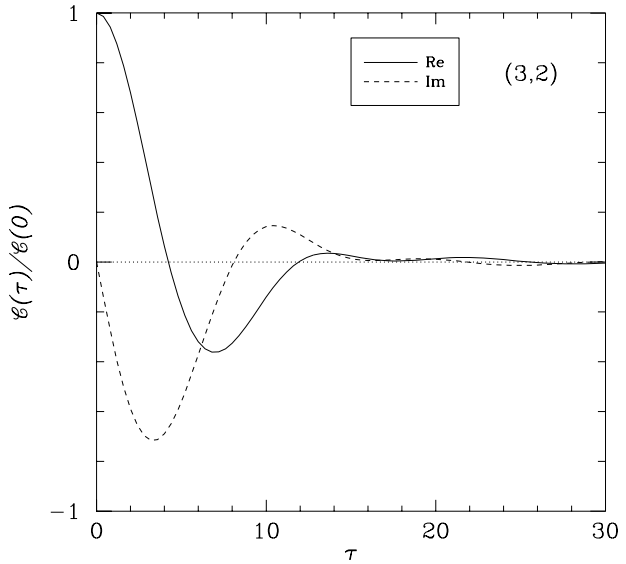

FIG. 12. Typical correlation function obtained by initializing the DIA with the spectrum of Fig. 5.

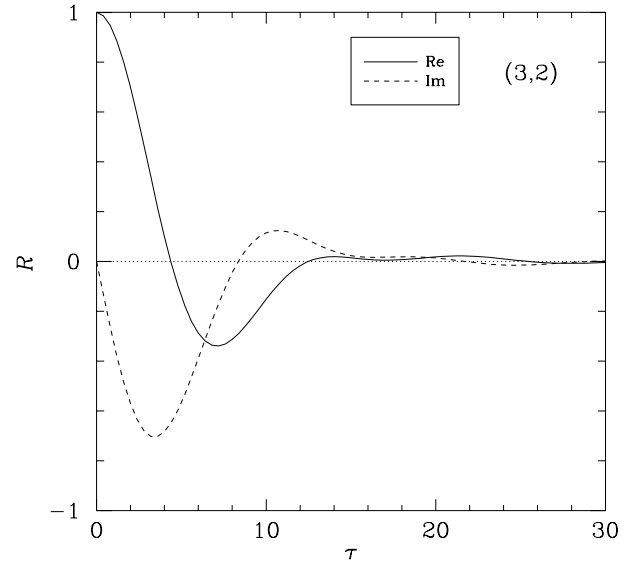

FIG. 13. Typical response function obtained by initializing the DIA with the spectrum of Fig. 5.

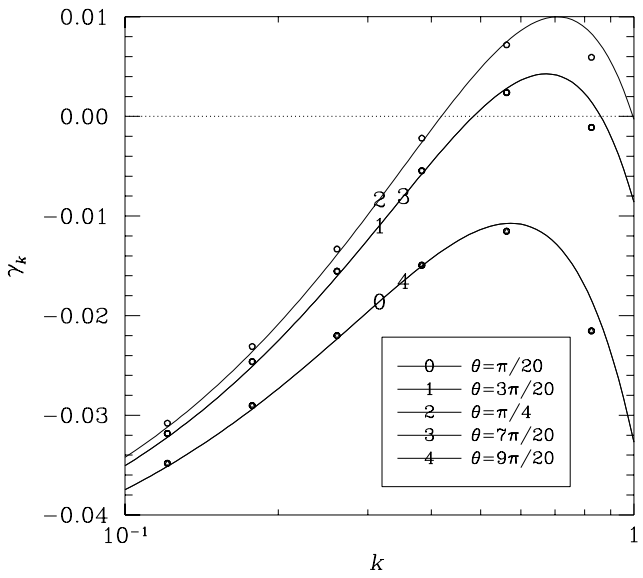

FIG. 14. Growth rate used by Waltz.

$$-0.5\left(\frac{|k_y|-0.5}{0.5}\right)^2\Bigg] - 0.05. \tag{49}$$

This function is illustrated in Fig. 14. It reaches its maximum value of 0.01 at $(k_x, k_y) = (0.5, 0.5)$ and is damped at both high and low k. The frequency $ik_yV_{\rm d}/(1+k^2)$ is shown in Fig. 15. The symbols on these plots indicate the value of the functions at the bin centers, for a (relatively coarse) 6×20 polar bin geometry. Although the reality condition $\psi_{\boldsymbol{k}} = \psi^*_{-\boldsymbol{k}}$ is exploited to reduce the number of modes, we do not make explicit use of the additional symmetry $k_x \to -k_x$ (for fixed k_y).

Waltz[46] applied the quasistationary EDQNM equations to Eqs. (48) and (49); in a steady state, these agree with the RMC equations.[47] Using a 10×20 polar bin geometry from $k = 0.1$ to $k = 1.0$, we solved both the RMC and RTFM for this problem. The RMC was successfully evolved from a statistical equilibrium distribution to the stationary state depicted in Fig. 16. This anisotropic closure computation required 31 CPU minutes on a Sun Ultra-1 SparcStation, to be compared with 43 minutes on a CRAY J90 for a conventional 32×32 simulation, also graphed in Fig. 16. The bin averaging for the 68 360 distinct triads required only 36 CPU seconds. This comparison demonstrates that the computational advantages of statistical closures are not limited to the case of isotropic turbulence. In Fig. 17, we graph the anisotropy of the energy spectrum. In contrast to Fig. 9, we see that the anisotropy is large and enters over a broad range of wave numbers.

We found that for this case the RTFM did not relax to a steady solution; instead, it appeared to oscillate between two states. The RTFM solution plotted in Fig. 16 corresponds to the state with the maximum energy. It

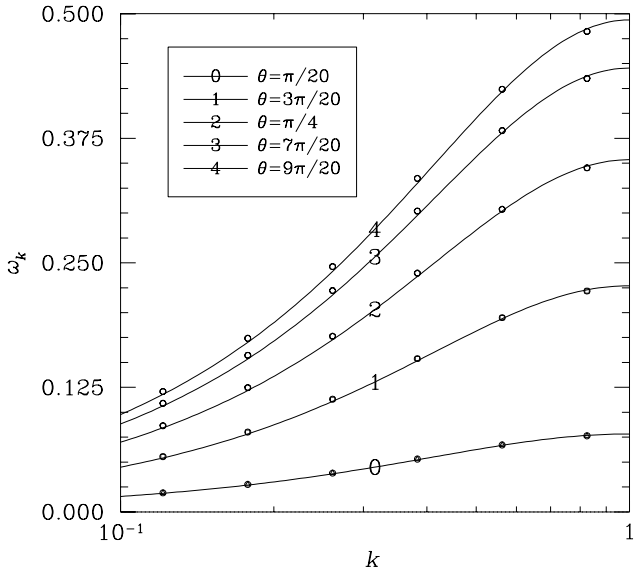

FIG. 15. Frequency $ik_yV_{\rm d}/(1+k^2)$.

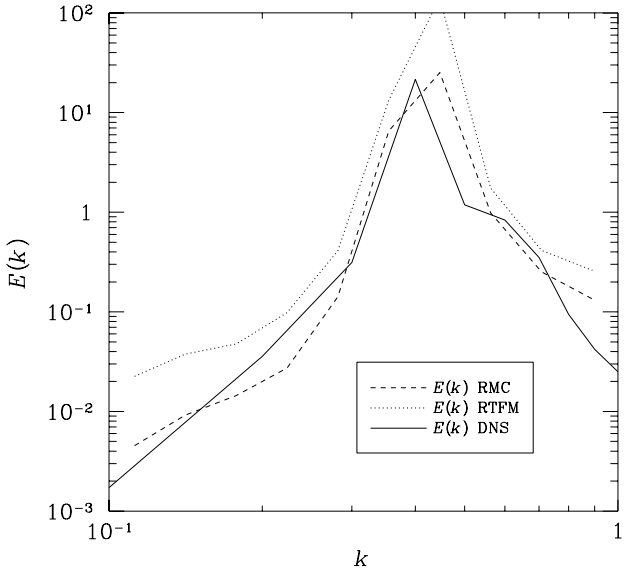

FIG. 16. Energy spectra predicted by the RMC, RTFM and DNS for Waltz's case.

was verified that the TFM also exhibits these oscillations when applied to this problem. Overall, it would appear that the RMC is a better candidate than the more heuristic TFM/RTFM for describing the statistical properties of broad-band turbulence, where no inertial range is expected and random Galilean invariance is not an issue.

A. Wave-number scaling of the nonlinear damping

In Fig. 18 we depict the angle-averaged scaling of $\widehat{\eta}_{\boldsymbol{k}} \doteq \eta_{\boldsymbol{k}} - \nu_{\boldsymbol{k}}$ with k for Waltz's case, as computed by the RMC. At the long wavelengths, the arguments of Dupree[48] might lead one to the (incorrect) scaling[49]

$$\widehat{\eta}_{\boldsymbol{k}} \sim k^4 D. \tag{50}$$

Krommes *et al.*[50] have shown that Eq. (50) results from retaining only the terms that correspond to a passive approximation. In contrast, a fully self-consistent analysis based on a Markovian closure may be used to deduce the approximate scaling relation

$$\widehat{\eta}_{\boldsymbol{k}} \sim \begin{cases} -k^3 k_0 D & \text{for } k \ll k_0, \\ kV_E & \text{for } k \gg 1. \end{cases} \tag{51}$$

Here, k_0 represents a characteristic energy-containing wave number less than 1 and V_E represents the $E\times B$ velocity. We see from Fig. 16 that $k_0 \approx 0.4$ for our case.

The negative value of the predicted $\widehat{\eta}_{\boldsymbol{k}}$ at small wave numbers represents nonlinear forcing. In Fig. 18, we see that $\widehat{\eta}_{\boldsymbol{k}}$ is indeed negative for small k and increases roughly linearly as k is increased, as expected from Eq. (51) and contrary to Eq. (50).

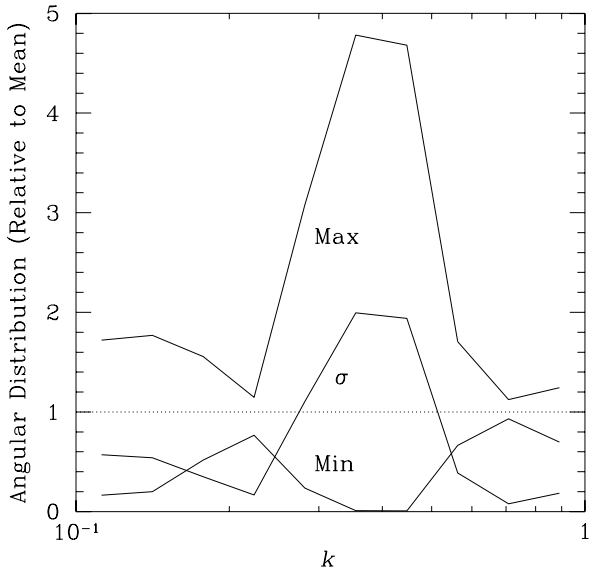

FIG. 17. Anisotropy of the RMC energy spectrum in Fig. 16.

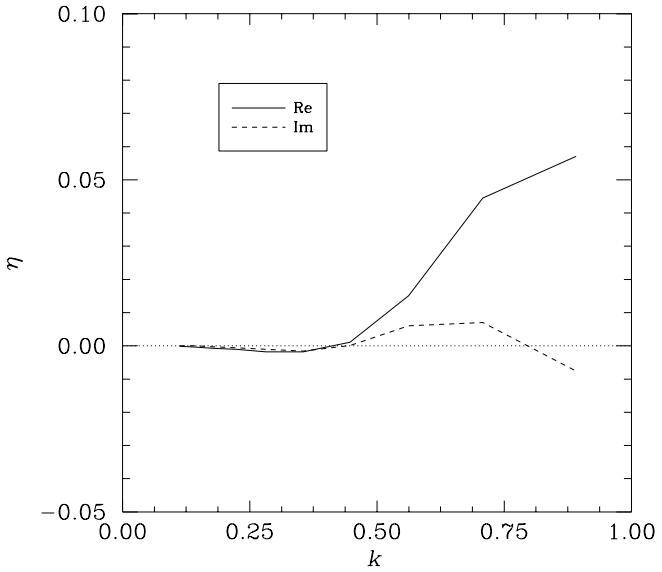

FIG. 18. Scaling of $\widehat{\eta}_{\boldsymbol{k}}$ *vs.* k for the RMC solution in Fig. 16.

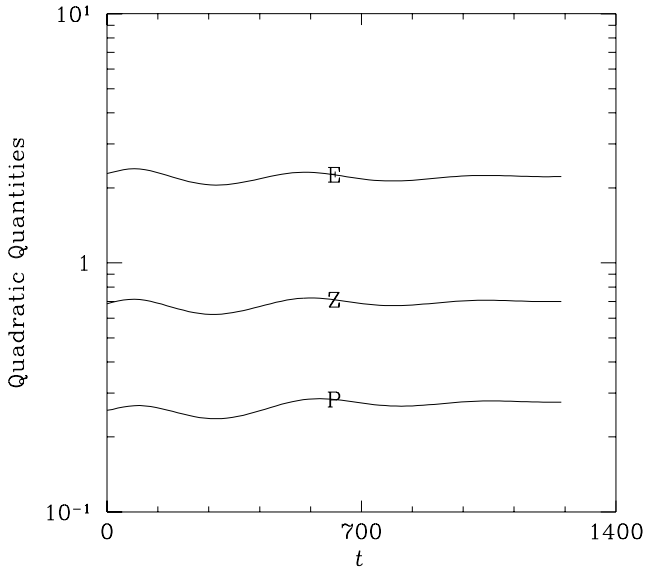

FIG. 19. Saturation of the DIA for Waltz's case.

Note that in a true enstrophy inertial range, the scaling $\widehat{\eta}_{\boldsymbol{k}} \sim k$ would differ from the scaling for the turnover time $\tau_{\rm eddy} \doteq \ell/u$: from the relation $u^2 \sim kE(k) \sim k^{-2}$, it follows that $\tau_{\rm eddy}$ is roughly independent of wave number. In the RTFM, this distinction, between the turnover rate $\eta^{\rm S}_{\boldsymbol{k}} \sim \tau^{-1}_{\rm eddy}$ and the predicted nonlinear damping rate $\eta_{\boldsymbol{k}}$, is fundamental to the issue of random Galilean invariance; a demonstration of the $\eta^{\rm S}_{\boldsymbol{k}}$ scaling is given in Ref. 24.

B. Two-time statistics

We were able to obtain a stationary DIA solution for a 6×20 bin geometry by using a steady-state 6×20 RMC solution as an initial condition. The saturation of the energy E, enstrophy Z, and palinstrophy P, defined by

$$E \doteq \tfrac{1}{2} \sum_{\boldsymbol{k}} k^2 \langle |\psi_{\boldsymbol{k}}|^2 \rangle, \tag{52a}$$

$$U \doteq \tfrac{1}{2} \sum_{\boldsymbol{k}} k^4 \langle |\psi_{\boldsymbol{k}}|^2 \rangle, \tag{52b}$$

$$P \doteq \tfrac{1}{2} \sum_{\boldsymbol{k}} k^6 \langle |\psi_{\boldsymbol{k}}|^2 \rangle, \tag{52c}$$

is depicted in Fig. 19. In this run, 21 040 triads were evolved 250 time steps (1.3 CPU hours on a Sun Ultra-1 SparcStation) to obtain the final energy spectrum depicted in Fig. 20. This result demonstrates that it is numerically feasible to integrate the DIA for anisotropic two-dimensional turbulence even in the presence of many interacting modes.

Sample correlation- and response-function data are illustrated in Figs. 21 and 22. We note that although these statistical quantities do not satisfy the FD relation perfectly (since a saturated turbulent state is not a thermodynamic equilibrium), there is still a qualitative correspondence between their temporal behaviors.

VIII. DISCUSSION

In this work we proposed a new closure, the realizable test-field model (RTFM), to overcome a flaw of the test-field model in the presence of linear waves: namely, the possibility that predicted energies can become negative, as illustrated in Fig. 1. This closure was applied to obtain statistical solutions of the Charney–Hasegawa–Mima equation. Because the linear wave term in this equation is anisotropic, it was necessary to develop a generalization of the isotropic wave-number partitioning scheme discussed in Ref. 22. With this technique, which affords a dramatic reduction in the number of retained Fourier modes, it was possible to apply the RTFM to obtain saturated states of drift-wave turbulence in two dimensions. The results were compared with those obtained using direct numerical simulation and also with two alternative closures, the RMC and the related DIA.

Another contribution of this work was the extension of Kraichnan's test-field model to situations more general than the isotropic Navier–Stokes turbulence for which it was originally constructed. While the test-field procedure is clear for cases of pure advection, we remark that it may lose at least its intuitive content in more complicated situations of arbitrary (e.g., complex) mode-coupling coefficients. What can be said in defense of the general

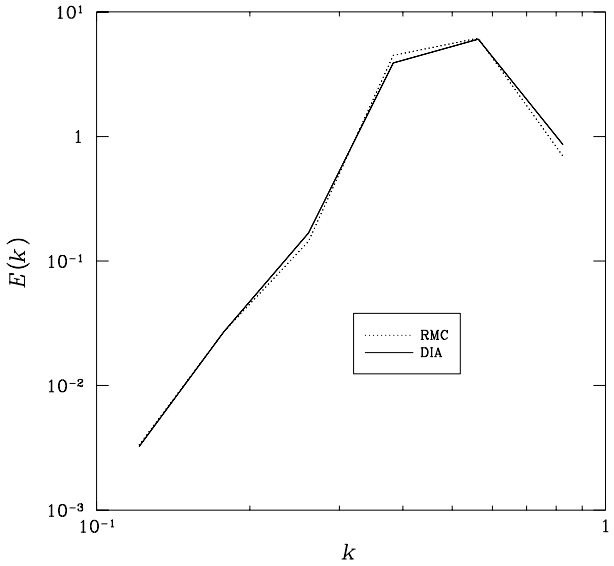

FIG. 20. Comparison of the RMC and DIA energy spectra for Waltz's case, using a 6×20 bin geometry.

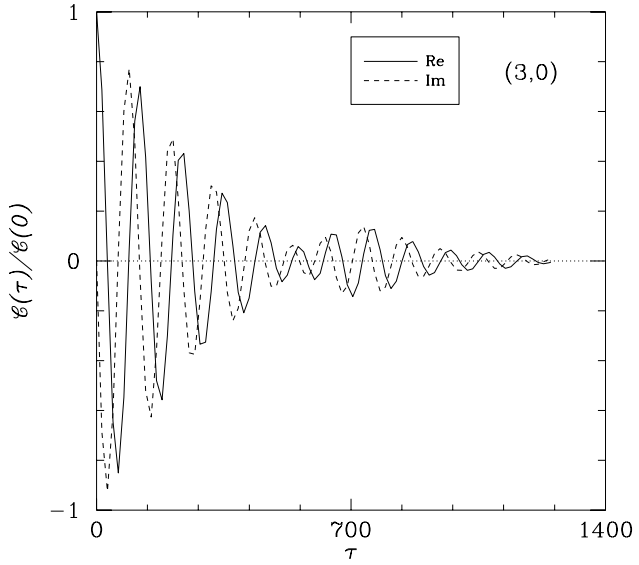

FIG. 21. Typical correlation function obtained by applying the DIA to Waltz's case.

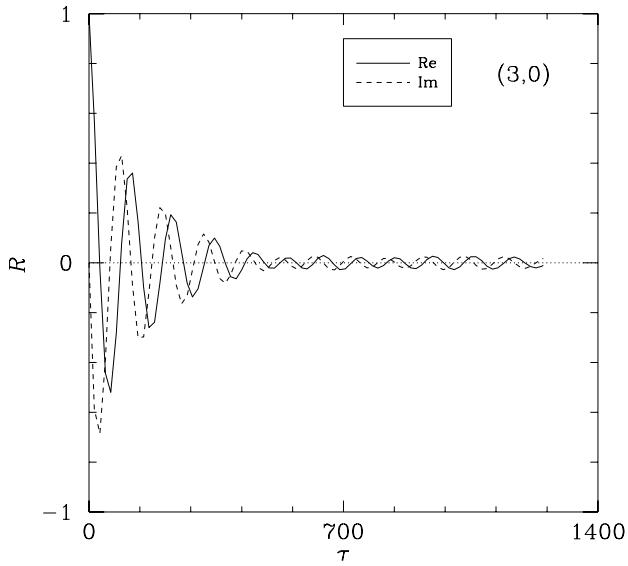

FIG. 22. Typical response function obtained by applying the DIA to Waltz's case.

procedure described in Sec. III is that it leads to random Galilean invariant-modifications, Eqs. (19) and Eqs. (40), of the original closure equations.

In a comparison of closure solutions to conventional numerical simulation data for a special case of the Hasegawa–Mima problem, reasonable agreement was obtained. The dual-cascade scenario was demonstrated by examining the energy and enstrophy transfer functions. With the closure solutions, we also examined the degree of anisotropy in these problems: in the Hasegawa–Mima equation, anisotropy enters only at the long wavelengths.

In addition, we obtained DIA solutions for which the correlation and response functions were found to be in good correspondence with the FD relation. With the RMC, we obtained a scaling for the nonlinear damping coefficients $\widehat{\eta}_{\boldsymbol{k}}$ that contradicts simple passive estimates but is in reasonable qualitative agreement with analytical estimates of the self-consistent closure predictions.

It is worth mentioning an alternative to the anisotropic wave-number partitioning scheme developed in this work. Herring[35] expanded the statistical variables in Fourier harmonics of the polar angle. If the turbulence is considered to be approximately isotropic, one can obtain an accurate representation by truncating the Fourier series at low order. In the bin procedure this would correspond to using only a few angular partitions. It would be useful to compare the advantages and disadvantages of the two approaches. It is likely that one method will be more accurate than the other for certain specific angular distributions; however, it has not yet been established in general which procedure can most probably achieve a given accuracy with the least computational effort.

Finally, let us comment on a possible use of the RTFM. It is occasionally asserted that a violation of ran-

dom Galilean invariance should not materially affect the computation of plasma transport coefficients (e.g., see Ref. 27). Detailed comparisons of the RMC and RTFM solutions could be used to test this assertion for drift-wave problems more realistic than the ones presented here. If this turns out to be generally true, then systematically derived DIA-based statistical closures like the RMC may turn out to be useful tools for investigating plasma turbulence, despite their incorrect treatment of inertial-range dynamics.

ACKNOWLEDGMENTS

The authors would like to thank Maurizio Ottaviani, Neil Pomphrey, and Steven Orszag for their comments on a preliminary version of this work, Leaf Turner for providing us with copies of his work prior to publication, and Jackson Herring for useful remarks on the anisotropic test-field model. Support from U.S. Department of Energy Contract Nos. DE–AC02–76CHO3073 and DE–FG05–80ET–53088 and the Natural Sciences and Engineering Research Council of Canada is gratefully acknowledged. The computations were performed at the Max-Planck-Institut für Plasmaphysik.

A portion of this work is based on a thesis submitted to Princeton University in partial fulfillment of the requirements for the degree of Doctor of Philosophy.[25]

APPENDIX A: GEOMETRIC WEIGHT FACTORS IN POLAR COORDINATES

We now present a general anisotropic algorithm for evaluating the geometry weight factors in Eq. (43). Upon transforming the angular variables of integration to $\bar{\alpha} \doteq \alpha - \alpha_<$ and $\bar{\beta} \doteq \beta - \beta_<$ and defining $\Delta\alpha \doteq \alpha_> - \alpha_<$ and $\Delta\beta \doteq \beta_> - \beta_<$, we evaluate the innermost two integrals of Eq. (43) to obtain

$$\int_{k_<}^{k_>} k\,dk \int_0^{\Delta\alpha} d\bar{\alpha} \int_{p_<}^{p_>} p\,dp \int_0^{\Delta\beta} d\bar{\beta}\ [\mathrm{H}(q_> - |\boldsymbol{k}+\boldsymbol{p}|) - \mathrm{H}(q_< - |\boldsymbol{k}+\boldsymbol{p}|)]$$
$$\times [\mathrm{H}(\gamma_> - \mathrm{Arg}(-\boldsymbol{k}-\boldsymbol{p})) - \mathrm{H}(\gamma_< - \mathrm{Arg}(-\boldsymbol{k}-\boldsymbol{p}))]\ f(\boldsymbol{k},\boldsymbol{p},-\boldsymbol{k}-\boldsymbol{p}), \tag{A1}$$

where Arg denotes the principal branch, taken in the interval $[0, 2\pi)$. Without loss of generality, we order the variables so that $\Delta\beta \geq \Delta\alpha$. In terms of new angular variables $\bar{r} \doteq \bar{\beta} - \bar{\alpha}$ and $\bar{\alpha}$ and upon denoting $f(k,p,\bar{r},\bar{\alpha}) \doteq f(\boldsymbol{k},\boldsymbol{p},-\boldsymbol{k}-\boldsymbol{p})$, one may rewrite the integral as

$$\int_{p_<}^{p_>} p\,dp \int_{k_<}^{k_>} k\,dk \int_{-\Delta\alpha}^{\Delta\beta} d\bar{r}\ [\mathrm{H}(q_> - |\boldsymbol{k}+\boldsymbol{p}|) - \mathrm{H}(q_< - |\boldsymbol{k}+\boldsymbol{p}|)]$$
$$\times \int_{\bar{\alpha}_<(\bar{r})}^{\bar{\alpha}_>(\bar{r})} d\bar{\alpha}\ [\mathrm{H}(\gamma_> - \mathrm{Arg}(-\boldsymbol{k}-\boldsymbol{p})) - \mathrm{H}(\gamma_< - \mathrm{Arg}(-\boldsymbol{k}-\boldsymbol{p}))]\ f(k,p,\bar{r},\bar{\alpha}). \tag{A2}$$

Here

$$\bar{\alpha}_<(\bar{r}) \doteq \begin{cases} 0 & \text{if } \bar{r} \geq 0, \\ -\bar{r} & \text{if } \bar{r} < 0, \end{cases} \tag{A3}$$

$$\bar{\alpha}_>(\bar{r}) \doteq \begin{cases} \Delta\beta - \bar{r} & \text{if } \bar{r} \geq \Delta\beta - \Delta\alpha, \\ \Delta\alpha & \text{if } \bar{r} < \Delta\beta - \Delta\alpha. \end{cases} \tag{A4}$$

A particular branch of $\mathrm{Arg}(-\boldsymbol{k} - \boldsymbol{p})$ is given by

$$\arg(-\boldsymbol{k} - \boldsymbol{p}) = \alpha + \theta, \tag{A5}$$

where, in terms of $r \doteq \beta - \alpha = \bar{r} + \beta_< - \alpha_<$,

$$\theta \doteq \Theta(-k - p\cos r, -p\sin r) \pmod{2\pi} \tag{A6}$$

and $\Theta(x, y)$ is any given branch of the generalized arctangent function:[51]

$$\Theta(x, y) \doteq \begin{cases} \arctan y/x & \text{if } x > 0, \\ \pi + \arctan y/x & \text{if } x < 0, \\ 0 & \text{if } x = 0. \end{cases} \tag{A7}$$

Thus one branch of the condition

$$\gamma_< \leq \arg(-\boldsymbol{k} - \boldsymbol{p}) \leq \gamma_> \tag{A8}$$

can be written

$$\gamma_< - \alpha_< - \theta \leq \bar{\alpha} \leq \gamma_> - \alpha_< - \theta. \tag{A9}$$

This enables one to do the $\bar{\alpha}$ integration immediately:

$$
\begin{aligned}
h(k,p,\bar{r}) &\doteq \int_{\bar{\alpha}_<(\bar{r})}^{\bar{\alpha}_>(\bar{r})} d\bar{\alpha}\ \left[\mathrm{H}\big(\gamma_> - \mathrm{Arg}(-\boldsymbol{k}-\boldsymbol{p})\big) - \mathrm{H}\big(\gamma_< - \mathrm{Arg}(-\boldsymbol{k}-\boldsymbol{p})\big)\right]\ f(k,p,\bar{r},\bar{\alpha}) \\
&= I\left[\min(\bar{\alpha}_>, \gamma_> - \alpha_< - \theta), \max(\bar{\alpha}_<, \gamma_< - \alpha_< - \theta)\right] \\
&\qquad + I\left[\min(\bar{\alpha}_>, \gamma_> - \alpha_< - \theta + 2\pi), \max(\bar{\alpha}_<, \gamma_< - \alpha_< - \theta + 2\pi)\right] \\
&\qquad + I\left[\min(\bar{\alpha}_>, \gamma_> - \alpha_< - \theta + 4\pi), \max(\bar{\alpha}_<, \gamma_< - \alpha_< - \theta + 4\pi)\right], \qquad \text{(A10)}
\end{aligned}
$$

where $I[b,a] \doteq H(b-a)\,[g(k,p,\bar{r},b) - g(k,p,\bar{r},a)]$ and

$$g(k,p,\bar{r},a) \doteq \int_0^a d\bar{\alpha}\, f(k,p,\bar{r},\bar{\alpha}). \tag{A11}$$

The latter integral is computed analytically and coded as a subroutine. For example, in the (usual) case where f is isotropic one obtains $g(k,p,\bar{r},a) = af(k,p,\bar{r},0)$. The 2π and 4π offsets of the second and third terms of $h(k,p,\bar{r})$ correctly yield the principal branch (Arg), assuming that the angular variables here are taken between 0 and 2π. (These offsets arise from the observation that if $\alpha \in [0,2\pi]$ and $\beta \in [0,2\pi]$, then $\alpha - \beta \in [-2\pi, 2\pi]$, etc.) The problem has thus been reduced to a three-dimensional integration over p, k, and $\bar{r}$.

The Heaviside restrictions on $|\boldsymbol{k}+\boldsymbol{p}|$ can be transformed into restrictions on the limits of the $\bar{r}$ integration, eliminating unnecessary integration when the $\bar{r}$ integrand is zero due to the magnitude restriction. For fixed p and k, one solves the relations

$$q_>^2 = k^2 + p^2 + 2kp\cos r_{2,3}, \tag{A12a}$$

$$q_<^2 = k^2 + p^2 + 2kp\cos r_{1,4} \tag{A12b}$$

for the r's, taking them to lie in $[0,2\pi]$. The magnitude restriction is then equivalent to the requirement that the principal angle of $r \doteq \beta - \alpha$ lies in $[r_1, r_2]$ or $[r_3, r_4]$. Next, one computes $\bar{r}_{1,2} = r_{1,2} - r_{\text{off}}$, where r_{off} is the principal angle of $\beta_< - \alpha_<$, adjusting $\bar{r}_1$ and $\bar{r}_2$ to lie between $[0,2\pi]$ if possible. (Otherwise, if $\bar{r}_1 < 0 < \bar{r}_2$, the interval $[\bar{r}_1, \bar{r}_2]$ is split into $[0,\bar{r}_2]$ and $[2\pi+\bar{r}_1, 2\pi]$ and the following procedure is applied to each sub-interval.) The $\bar{r}$ integral then becomes

$$\left(\int_{\max(\Delta\beta-\Delta\alpha,\bar{r}_1)}^{\min(\Delta\beta,\bar{r}_2)} d\bar{r} + \int_{\max(0,\bar{r}_1)}^{\min(\Delta\beta-\Delta\alpha,\bar{r}_2)} d\bar{r} + \int_{\max(-\Delta\alpha,\bar{r}_1-2\pi)}^{\min(0,\bar{r}_2-2\pi)} d\bar{r}\right) h(k,p,\bar{r}). \tag{A13}$$

This procedure is repeated for the $[\bar{r}_3, \bar{r}_4]$ interval as well. To get the final answer to Eq. (43), the sum of these two results is then multiplied by kp and integrated over k and p.

a. Numerical Considerations

Efficient numerical integration requires some analytical knowledge of the behavior of the integrand to determine the appropriate sampling resolution. An adaptive Simpson method is used to achieve a specified relative accuracy. To work correctly, the integration routine needs a resolution parameter $\Delta_{\max}$, which is set to the size of the smallest structure in the integrand.

There is a resolution requirement associated with the angular restriction in Eq. (A13). To circumvent this problem we make the stipulation, without loss of generality, that $\Delta\gamma \doteq \gamma_> - \gamma_<$ is larger than $\Delta\beta$ (and hence also $\Delta\alpha$). Then if $\text{Arg}(-\boldsymbol{k}-\boldsymbol{p})$ lies outside the interval $[\gamma_<, \gamma_>]$ for both the endpoint evaluations of the $\bar{r}$ integral, it will for every interior point as well, so the integral must vanish. Otherwise, the integrand will not vanish for at least one of the endpoints and the desired structure can be numerically resolved. With the above ordering, using the value $\Delta_{\max} = \pi$ for the $\bar{r}$ integration is sufficient to guarantee that the code samples the integrand with a sufficiently fine resolution.

It is not hard to show that the size of the smallest structure for the p and k integrals is about $q_> - q_<$. To see this, consider the extreme cases of the magnitude restriction $q_< \le |\boldsymbol{k}+\boldsymbol{p}| \le q_>$:

$$p_{2,3} = -k\cos r \pm \left(q_>^2 - k^2\sin^2 r\right)^{1/2}, \tag{A14a}$$

$$p_{1,4} = -k\cos r \pm \left(q_<^2 - k^2\sin^2 r\right)^{1/2}. \tag{A14b}$$

Note that $p_3 \le p_4 \le p_1 \le p_2$. The integrand is nonzero only on the intervals $[p_3, p_4]$ and $[p_1, p_2]$. The resolution is determined by the minimum value, over k and r, of

$$\Delta p \doteq p_4 - p_3 = p_2 - p_1 \ge q_> - q_<. \tag{A15}$$

The last inequality follows from the monotonicity of the function $f(x) \doteq (x^2 - a^2)^{1/2} - x$ for positive x. It is thus found that setting $\Delta_{\max}$ to less than $\frac{1}{2}(q_> - q_<)$ eliminates any resolution problems. (The factor of $\frac{1}{2}$ is needed since the structure could be split equally among two adjacent intervals used in the numerical integration.) In the code $\Delta_{\max}$ is set to $0.4(q_> - q_<)$ for both the p and k integrals.

APPENDIX B: NUMERICAL CODE

The numerical computations in this work were performed with the multipurpose code `DIA`.[28,29,25] It is designed around a general kernel that implements the DIA, EDQNM, RMC, TFM, and RTFM for the generic n-field system

$$\frac{\partial}{\partial t}\psi^\alpha + \nu^\alpha{}_\mu \psi^\mu = \tfrac{1}{2}\sum_\Delta M^\alpha{}_{\beta\gamma}\psi^{\beta *}\psi^{\gamma *}. \tag{B1}$$

The code may be tailored to a wide class of physics problems, including those involving inhomogeneities, kinetic descriptions, or three-dimensional dynamics, by specifying routines to compute the coefficients $\nu^\alpha{}_\mu$ and $M^\alpha{}_{\beta\gamma}$. In Part I of this work, we used this same code to apply closures to study systems of three interacting waves.

The basic time-stepping algorithm is a predictor–corrector scheme that is formally accurate to second order in the time step Δt. For the DIA, we employ the same scheme used by Kraichnan.[52] This semi-implicit method

guarantees exact energy conservation by the nonlinear terms and preserves the inviscid equilibrium solutions that are discussed in Appendix D of Part I. It is used to evolve the energy equation of all three closures and also to compute the DIA response function. The scheme that advances the quantity $\Theta_{\boldsymbol{kpq}}$ of the RMC solves for the evolution on the linear time scale exactly. For the EDQNM closure, a different algorithm that exploits the Markovian form of the evolution equation is used for advancing $\theta_{\boldsymbol{kpq}}$ in a manner that numerically guarantees the non-negativity of $\theta_{\boldsymbol{kpq}}$ in the wave-free case.[53]

The use of a variable time step is advantageous for problems involving growing amplitudes, in which the nonlinear time scale becomes progressively shorter as the run proceeds. We have incorporated a mechanism that automatically adjusts the time step dynamically based on stability considerations without user intervention. The two stages of the predictor–corrector algorithm provide a convenient means of dynamically estimating the numerical error. We define the error in any particular time step t to be

$$\epsilon(t) \doteq \max\left\{\frac{|P(t)-C(t)|}{\max\left[|C(t)|,|C(t-\Delta t)|\right]}\right\}, \qquad \text{(B2)}$$

where $P(t)$ is the predicted value of some quantity and $C(t)$ is the corrected value. The outer maximum is taken over all explicitly evolved variables but not over derived variables such as η. The previous value $C(t-\Delta t)$ is used to assist the time-stepping mechanism during the transition of a quantity through zero.[54]

The user specifies two parameters that must bound the above error:

$$\mathrm{tol}_{\min} \le \epsilon \le \mathrm{tol}_{\max}. \qquad \text{(B3)}$$

If the inequality on the left (right) is violated, the time step is multiplied (divided) by a user-specified factor. By leaving the choice of the two tolerance parameters up to the user, this scheme effectively avoids all of the complications associated with the estimation of numerical stability.[55]

---

[1] R. H. Kraichnan, Phys. Rev. **109**, 1407 (1958).
[2] R. H. Kraichnan, J. Fluid Mech. **5**, 497 (1959).
[3] R. H. Kraichnan, J. Math. Phys. **2**, 124 (1961).
[4] D. C. Leslie, *Developments in the Theory of Turbulence* (Clarendon Press, Oxford, 1973).
[5] J. A. Krommes, in *Handbook of Plasma Physics*, edited by M. N. Rosenbluth and R. Z. Sagdeev (North-Holland, Amsterdam, 1984), Vol. 2: *Basic Plasma Physics II*, edited by A. A. Galeev and R. N. Sudan, Chap. 5.5, pp. 183–268.
[6] J. C. Bowman, J. A. Krommes, and M. Ottaviani, Phys. Fluids B **5**, 3558 (1993).
[7] A closure is said to be realizable if there exists an underlying probability density function for the statistics it predicts.
[8] R. H. Kraichnan, in *Theoretical Approaches to Turbulence*, Vol. 58 of Applied Mathematical Sciences Series, edited by D. L. Dwoyer, M. Y. Hussaini, and R. G. Voigt (Springer, New York, 1985), Chap. V, p. 91.
[9] R. H. Kraichnan, J. Fluid Mech. **47**, 513 (1971).
[10] R. H. Kraichnan, J. Fluid Mech. **56**, 287 (1972).
[11] R. H. Kraichnan, Phys. Fluids **8**, 575 (1965).
[12] Y. Kaneda, J. Fluid Mech. **107**, 131 (1981).
[13] J. Qian, Phys. Fluids **26**, 2098 (1983).
[14] V. Belinicher and V. L'vov, Sov. Phys., JETP **66**, 303 (1987).
[15] R. H. Kraichnan, Phys. Fluids **9**, 1728 (1966).
[16] J. R. Herring and R. H. Kraichnan, J. Fluid Mech. **91**, 581 (1979).
[17] S. V. Bazdenkov and N. N. Kukharkin, Phys. Fluids A **5**, 2248 (1993).
[18] A. Hasegawa and K. Mima, Phys. Rev. Lett. **39**, 205 (1977).
[19] A. Hasegawa and K. Mima, Phys. Fluids **21**, 87 (1978).
[20] J. G. Charney, Geof. Publ. **XVII**, 3 (1948).
[21] C. E. Leith and R. H. Kraichnan, J. Atmos. Sci. **29**, 1041 (1972).
[22] J. C. Bowman, J. Sci. Comput. **11**, 343 (1996).
[23] A. Pouquet, M. Lesieur, J. C. André, and C. Basdevant, J. Fluid Mech. **72**, 305 (1975).
[24] J. C. Bowman, J. Fluid Mech. **306**, 167 (1996).
[25] J. C. Bowman, Ph.D. thesis, Princeton University, Princeton NJ, USA, 1992.
[26] G. Hu, J. A. Krommes, and J. C. Bowman, Phys. Lett. A **202**, 117 (1995).
[27] G. Hu, J. A. Krommes, and J. C. Bowman, Phys. Plasmas **4**, 2116 (1997).
[28] J. A. Krommes and J. C. Bowman, Bull. Am. Phys. Soc. **33**, 2022 (1988).
[29] J. C. Bowman and J. A. Krommes, Bull. Am. Phys. Soc. **33**, 2022 (1988).
[30] G. Holloway and M. C. Hendershott, J. Fluid Mech. **82**, 747 (1977).
[31] This is apparent even from a heuristic renormalization (resonance broadening) of the δ function in the wave kinetic equation to a Lorentzian.
[32] The quasistationary formulation used in Ref. 30 does not ensure that the transient energies are non-negative since η can achieve negative values during the evolution.
[33] R. H. Kraichnan, Phys. Fluids **6**, 1603 (1963).
[34] There is a typographical error in the triad assignments given in Ref. 33.
[35] J. R. Herring, J. Atmos. Sci. **32**, 2254 (1975).
[36] L. Turner, EDQNM Model of Evolution of Homogeneous Anisotropic Turbulence in a Helicity Representation, Technical Report No. LA-UR-96-618, Los Alamos National Laboratory, submitted to J. Fluid Mech.
[37] G. R. Newman and J. R. Herring, J. Fluid Mech. **94**, 163 (1979).
[38] M. Larcheveque, J. P. Chollet, J. R. Herring, M. Lesieur, G. R. Newman, and D. Schertzer, in *Turbulent Shear Flows*, edited by L. J. S. Bradbury, F. Durst, B. E. Launder, F. W. Schmidt, and J. H. Whitelaw (Springer, New York, 1980), Vol. 2, pp. 50–65.

[39] J. R. Herring and R. M. Kerr, J. Fluid Mech. **118**, 205 (1982).
[40] J. R. Herring, D. Schertzer, M. Lesieur, G. R. Newman, J. P. Chollet, and M. Larcheveque, J. Fluid Mech. **124**, 411 (1982).
[41] A. Hasegawa, C. G. Maclennan, and Y. Kodama, Phys. Fluids **22**, 2122 (1979).
[42] M. Ottaviani, J. C. Bowman, and J. A. Krommes, Phys. Fluids B **3**, 2186 (1991).
[43] A more sophisticated technique for extending the computational power of the DIA, which partially accounts for the non-Gaussian statistics predicted during a previous evolution, has been developed in H. A. Rose, Physica D **14**, 216 (1985).
[44] The substantial memory requirements, roughly 200 Megabytes, make it difficult to continue the evolution without a dramatic decrease in the speed of the calculation because of the need to swap data to disk.
[45] W. P. Dannevik (private communication, 1990).
[46] R. E. Waltz, Phys. Fluids **26**, 169 (1983).
[47] Waltz describes the equations he solves as the result of applying a "resonance approximation" to "the DIA weak coupling theory". He also sometimes refers to these equations as the DIA itself; however they are really just a quasistationary version of the EDQNM closure.
[48] T. H. Dupree, Phys. Fluids **10**, 1049 (1967).
[49] This corresponds to the conventional k^2D scaling for the nonlinear damping rate as suggested by Dupree; here, an extra factor of k^2 appears because the fundamental nonlinear interaction arises from the polarization drift.
[50] J. A. Krommes, J. C. Bowman, and M. Ottaviani, Bull. Am. Phys. Soc. **35**, 1957 (1990).
[51] The value of Θ at the singular points $(0, y)$ is arbitrary since this corresponds to points in the integration that precisely satisfy $k = p \cos r$, which may be removed since the integrand is bounded.
[52] R. H. Kraichnan, Phys. Fluids **7**, 1030 (1964).
[53] The difference between this algorithm and the one used for the energy equation appears only above second order.
[54] If the error was computed solely by the ratio of the predictor–corrector difference to the current value of a corrected variable that happened to be passing through zero, this *relative* error could become arbitrarily large. The error is therefore computed with respect to both current and previous values; our formula removes the artifact just described by calculating a combination of relative and absolute errors.
[55] These tolerance parameters are chosen to yield an efficient evolution that does not become unstable. Of course, even if the evolution is stable, it may still be inaccurate; in this case the maximum error tolerance should be decreased. In practice, our convergence tests indicate that whenever the numerical scheme is stable, the results are sufficiently accurate, bearing in mind the inherent inaccuracies of statistical closures.